Charles University in Prague
Faculty of Mathematics and Physics

DOCTORAL THESIS

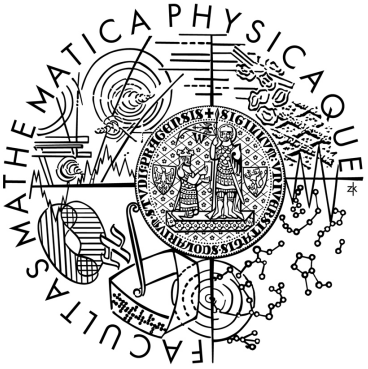

Radek Macháň

Supported Phospholipid Bilayers and their Interactions with Proteins Studied by Ellipsometry, Atomic Force Microscopy and Confocal Fluorescence Microscopy

J. Heyrovský Institute of Physical Chemistry of ASCR. v.v.i.

Supervisor: Prof. Martin Hof, DSc.

Study Programme: Physics
Study Branch: F4 – Biophysics, Chemical and Macromolecular Physics

Prague 2011

Acknowledgements:

I would like to express my gratitude to all people without whose help this thesis could have never been written. My thanks belong to my supervisor Prof. Martin Hof and to all members of his laboratory at J. Heyrovský Institute of Physical Chemistry, with whom I have had the pleasure to work. Names of most of them appear among authors of works, on which I, to a smaller or larger extent, participated. I also thank Dr. Pavel Janda from J. Heyrovský Institute of Physical Chemistry, who introduced me to the field of scanning probe microscopy. Special thanks belong to Prof. Wim Th. Hermens from Maastricht University and Delbia, b.v., from whom I have learned more than just ellipsometry and whom I admire for more than just his scientific merits.

I declare that I carried out this doctoral thesis independently, and only with the cited sources, literature and other professional sources.

I understand that my work relates to the rights and obligations under the Act No. 121/2000 Coll., the Copyright Act, as amended, in particular the fact that the Charles University in Prague has the right to conclude a license agreement on the use of this work as a school work pursuant to Section 60 paragraph 1 of the Copyright Act.

In Prague on the 20th of September 2011 *Radek Macháň*

Název práce: Podporované fosfolipidové dvojvrstvy a jejich interakce s proteiny studovaná pomocí elipsometrie, mikroskopie atomových sil a konfokální fluorescenční mikroskopie.

Autor: Radek Macháň

Katedra / Ústav: Ústav fyzikální chemie J. Heyrovského AV ČR, v.v.i.

Vedoucí disertační práce: prof. Martin Hof, DSc., Ústav fyzikální chemie J. Heyrovského AV ČR, v.v.i.

Abstrakt: Podporované lipidové dvojvrstvy sloužily jako umělý model biologických membrán při studiu membránové aktivity 5 vybraných antimikrobiálních peptidů. Hlavními experimentálními technikami byly elipsometrie, laserová řádkovací mikroskopie a fluorescenční korelační spektroskopie. Základní principy použitých experimentálních technik jsou vysvětleny v této práci s přihlédnutím k jejich stránkám podstatným pro charakterizaci lipidových dvojvrstev. Ve stručnosti je shrnut biologický význam antimikrobiálních peptidů a jejich působení na biologické membrány a jsou představeny základní vlastnosti vybraných peptidů. Následuje rozbor hlavních typů experimentálních studií a interpretace jejich výsledků. Morfologické změny lipidových dvojvrstev byly zkoumány elipsometrií a laserovou řádkovací mikroskopií. Nejzajímavější jevy byly pozorovány v případě melittinu, který vyvolal vznik dlouhých lipidových trubic vystupujících z dvojvrstvy. Laterální difúze lipidů měřená fluorescenční korelační spektroskopií vypovídá o uspořádání dvojvrstvy na vzdálenostech pod rozlišením optické mikroskopie.

Klíčová slova: lipidové membrány, antimikrobiální peptidy, fluorescenční korelační spektroskopie, difúze molekul

Title: Supported Phospholipid Bilayers and their Interactions with Proteins Studied by Ellipsometry, Atomic Force Microscopy and Confocal Fluorescence Microscopy.

Author: Radek Macháň

Department / Institute: J. Heyrovský Institute of Physical Chemistry of ASCR, v.v.i.

Supervisor: Prof. Martin Hof, DSc., J. Heyrovský Institute of Physical Chemistry of ASCR, v.v.i.

Abstract: Supported lipid bilayers have been used as an artificial model of biological membranes and their interaction with 5 selected antimicrobial peptides was studied by several experimental techniques, mainly ellipsometry, laser scanning microscopy and fluorescence correlation spectroscopy. The thesis explains basic principles of the applied techniques focusing on their aspects relevant to characterization of lipid bilayers. The biological significance of antimicrobial peptides, their modes of interaction with membranes and the basic characteristics of the selected peptides are briefly discussed. The following text describes the main types of experimental studies performed and the interpretation of their results. Peptide-induced changes in lipid bilayer morphology were characterized by ellipsometry and laser scanning microscopy. Most interesting effects were observed in the case of melittin, which induced formation of long lipid tubules protruding from the bilayer. Lipid lateral diffusion measured by fluorescence correlation spectroscopy can provide information on bilayer organization on length-scales below resolution of optical microscopy.

Keywords: lipid membranes, antimicrobial peptides, fluorescence correlation spectroscopy, molecular diffusion

Contents

Introduction

The thesis presents results of my research related to the topic of supported lipid bilayers (SLBs) and their interaction with peptides belonging to the class of antimicrobial or cytolytic peptides. In my work, I combined several experimental techniques to characterize selected properties of SLBs and their changes induced by the investigated peptides. The topic is of considerable interest because, firstly, antimicrobial peptides (AMPs) have been attracting a lot of interest thanks to their potential pharmacological applications as efficient antibiotics with a further advantage of low tendency of bacteria to develop resistance against them [1-4], and, secondly, most experimental evidence proves that their interaction with biological membranes, of which supported lipid bilayers are a popular artificial model, is essential for the activity of almost all known AMPs [4-7]. Investigation of peptide-induced changes in biological membranes (or their artificial models) can, therefore, help to understand the mechanisms governing AMPs' biological activity and their selectivity against certain types of cells.

First chapter explains basic properties of SLBs and their relevance to biological membranes, which they should mimic; practical aspects of their formation are also mentioned. The following three chapters describe the three main experimental techniques used in this thesis, which are stated in its title, namely, ellipsometry, atomic force microscopy and confocal fluorescence microscopy (with emphasis on florescence correlation spectroscopy, which is also the main topic of the review added to the thesis as *Attachment I*). All three techniques have a wide range of applications in many fields of research resulting in a variety of their modalities and specialized approaches to suit particular types of experiments. Therefore, their discussion in the thesis cannot be complete and only the most basic general principles of the methods are explained, with emphasis on aspects relevant to characterization of SLBs, followed by particulars applying to experiments presented in the thesis. The last chapter introduces antimicrobial peptides and their biological significance and describes four studies on which this thesis is based and which investigate interaction of selected AMPs with model membranes. Articles presenting results of those studies are added to the thesis as *Attachments II – V*.

1. Supported lipid bilayers and biological membranes

1.1. Basic characteristics of biological membranes

Biological membranes are indispensable for existence of any living cell. They form the barriers which separate the cell interior and exterior and organelles from cytosol and, thus, play an essential role in maintaining a stable environment inside of cells. Apart from their compartmentalization function, membranes are also the site of a variety of fundamental biochemical processes in the cell; many proteins require the specific membrane environment for their proper folding and function, ionic gradients across membranes are an important energy source etc. [8, 9]. In spite of the variety of functions they perform in all types of cells, biological membranes share many common characteristics. They are composed of membrane proteins and lipids (phospholipids, sphingolipids and sterols). Although the mass fraction of proteins in some types of membranes can be relatively high, a lipid bilayer is the key structural component of any biological membrane. The bilayer structure is a result of the amphiphilic nature of phospholipids and sphingolipids, which are arranged in the bilayer with their polar headgroups facing outwards (towards aqueous environment) and their hydrophobic tails forming the bilayer interior (see figure 1.1). It provides the mechanical stability and basic physical properties characteristic for membranes [8, 10, 11]. Those include:

i) low permeability to ions and polar molecules, which results from the hydrophobic nature of the interior of a lipid bilayer. This property is essential for maintaining stable intracellular environment and ionic gradients across membranes. Transport of ions across membranes happens only via membrane proteins and is, therefore, controlled by the cell. Loss of membrane integrity, which increases its non-selective permeability, has fatal consequences for the cell [8, 12].

ii) asymmetry in lipid composition between the two leaflets of the lipid bilayer is characteristic for membranes of living cells. Maintaining of lipid asymmetry is facilitated by slow rates of transversal movement of lipids between the two leaflets, called flip-flop. Unless the rate of flip-flop is enhanced by specific proteins or membrane defects [13-15], the asymmetry can be maintained for up to several hours [16-18].

iii) fluidity; this term describes the fast lateral mobility of lipids in the plane of the

membrane. Its importance was pointed out by Singer and Nicolson in their fluid mosaic model of membranes [19]. Fluidity results in self-sealing ability of membranes, homogeneous lateral distribution of lipids and also in lateral mobility of other molecules (such as membrane proteins) incorporated in the membrane. It influences, thus, kinetics and mechanism of membrane-associated biochemical reactions. Membrane fluidity is closely related to lipid ordering (more ordered bilayer is less fluid), which can influence activity of membrane proteins via changes in lateral pressure within the membrane [20-22].

Later studies have shown that biological membranes are not laterally homogeneous, but contain domains differing in lipid and protein composition and also in fluidity [23-26]. The relation between lipid lateral mobility and kinetics of membrane-associated processes is, therefore, a much more complex problem. Membrane fluidity is, nevertheless, a key parameter for understanding functions of cellular membranes.

1.2. Biological membranes and their artificial models

As has been said above, lipid bilayers are the main building blocks, which, to a large extent, determine properties of biological membranes. The way how various compounds (for example toxins or AMPs) influence properties of lipid bilayers can elucidate their effects on biological membranes and, thus, in many cases their effects on the whole cells. For that reason, artificial lipid bilayers and their interaction with biologically active substances are frequently investigated. Experiments with artificial bilayers are easier than with living cells; their main advantage, however, lies in the possibility to control the lipid composition of the bilayer and, thus, its physical parameters such as electrostatic charge density or fluidity. Influence of those parameters on interaction with biologically active substances can be, therefore, studied in a systematic manner.

Preparation of artificial lipid bilayers is, in principal, a rather simple task, because membrane lipids in aqueous environment organize themselves spontaneously into a bilayer [11]. The process is driven by hydrophobic effect, which forces the amphiphilic lipid molecules to organize into a structure in which the hydrophobic lipid tails are shielded from water and polar lipid headgroups exposed to it. Depending on the shape of its molecule (the ratio between the hydrophobic part

volume and the headgroup area) the lipid preferentially forms bilayers (lamellar phase), micelles or inversed micelles (hexagonal phase). Biological membranes always contain a fraction of lipids preferring non-lamellar phases, which help to stabilize the membrane in locations with significant curvature and during processes locally disturbing lamellar structure (such as membrane fusion or endocytosis) [8].

The commonly used artificial lipid bilayer systems can be divided into two main classes:

i) liposomes, which are closed spheres made of lipid bilayers. They can be further divided to multilamellar vesicles (consisting of many concentric bilayer spheres) and unilamellar vesicles (a single bilayer sphere), which are further classified according to their size. Small unilamellar vesicles (SUVs) with diameters to approximately 50 nm, large unilamellar vesicles (LUVs) with diameters up to a few μm and giant unilamellar vesicles (GUVs) with diameters of the order of tens of μm (comparable in size to cells) differ in the type of assays in which they are predominantly used and in their preparation protocols [8, 27-30].

ii) planar bilayers are either free-standing or supported. Free-standing planar bilayers are usually spanning apertures in a septum [31, 32]. Because of their large diameters resulting in negligible local curvature, GUVs are also sometimes considered a type of free-standing planar bilayers (*Attachment I*). Supported lipid bilayers are adsorbed to the surface of a solid support [33, 34]. Supported bilayers are stable, easy to handle and convenient for characterisation by surface characterization techniques (such as ellipsometry or scanning probe microscopy). Their main disadvantage is the proximity of the solid support, which can influence bilayer properties. Advantages of supported and free-standing bilayers are, to some extent, combined in bilayers on porous supports [35, 36]. SLBs were the main membrane-mimetic system used in the studies presented in this thesis; therefore, their formation and properties are discussed in more detail in the next section.

1.3. Formation of supported lipid bilayers

Several methods have been proposed for formation of lipid bilayers on solid supports; the most common techniques are Langmuir-Blodgett deposition [34] and vesicle adsorption and rupture on hydrophilic surfaces [37, 38]. The letter approach was used in this work and will be, therefore, discussed more thoroughly. It is quite a

simple procedure since the bilayer is formed spontaneously when a suitable hydrophilic surface is exposed to a suspension of lipid vesicles. Although the preparation protocol has been used for many years, there remain aspects of the process of bilayer formation, which have not been fully explained. Main features of several models, which have been proposed to describe the process, are shown in figure 1.1.

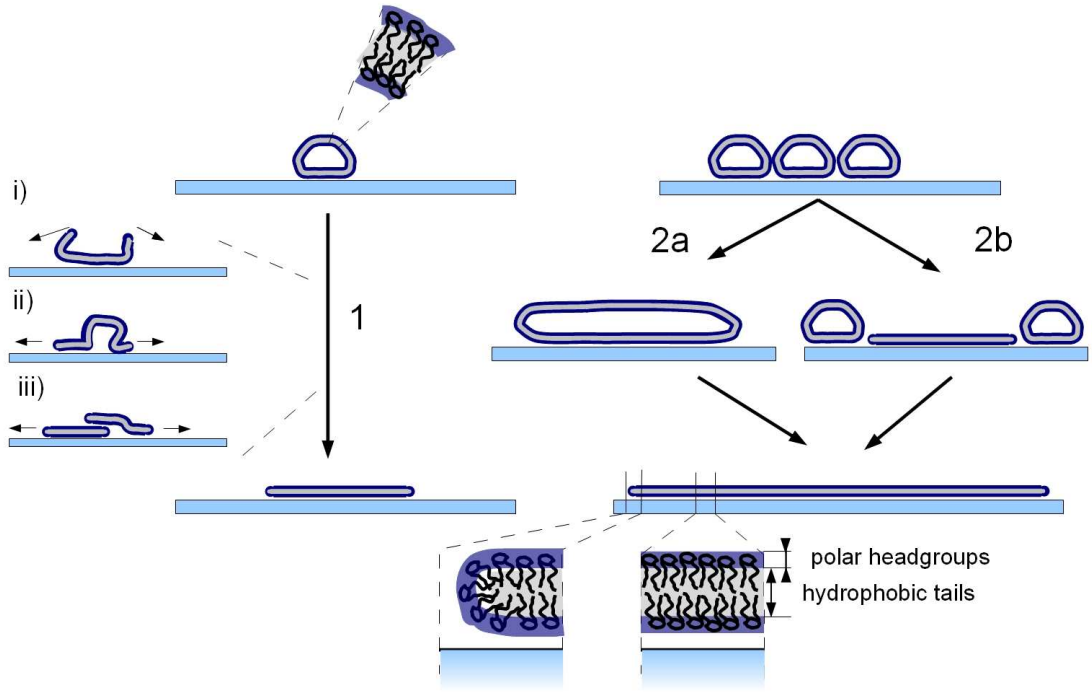

Figure 1.1: Schematic depiction of tentative pathways of SLB formation by adsorption and rupture of vesicles on hydrophilic solid supports. Either each individual vesicle ruptures upon its adsorption to the surface forming a small bilayer patch (**1**) or interaction of several vesicles adsorbed to the surface in close proximity to each other is needed to induce rupture (**2**). In the latter case, several vesicles may fuse together prior to rupture (**2a**) or collective effect of neighbouring vesicles leads to the rupture of the first vesicle and the edge of the resulting bilayer patch induces rupture of adjacent vesicles (**2b**). Several mechanisms of vesicle rupture (applying to both pathways **1** and **2**) have been proposed. They differ mainly in prediction which leaflet of the vesicle membrane is proximal to the solid support, whether **i)** the outer, **ii)** the inner or **iii)** a mixture of both.

Whether a lipid bilayer is formed on the support and the actual pathway, which the bilayer formation follows, is determined mainly by the interplay between

bilayer-support interactions (the adhesion energy between the bilayer and the support) and mechanical properties of the bilayer (its bending modulus, curvature strain). The transition from a vesicle to a bilayer patch is favourable in terms of adhesion energy (due to increased contact area between lipids and support), but unfavourable in terms of vesicle curvature energy [39-41]. The edge of the bilayer patch is also energetically unfavourable (because of its high local curvature) and certainly represents a factor acting against rupture [42]. Therefore, only bilayer patches larger than a certain critical area (which depends on lipid and support properties) are energetically favourable and, thus, formed [40]. If individual vesicles are not big enough to produce patches of sufficient size, rupture can proceed only via collective effects of several adjacent vesicles. That explains the need for so called critical coverage in some cases of SLB formation [43-45]. The surface is, in those cases, covered by a layer of adsorbed vesicles and, only after a certain critical coverage of the surface by vesicles has been reached, rupture starts and SLB is formed. An example of experimental observation of SLB formation proceeding via critical coverage is described in section 2.3.

Adhesion energy between the bilayer and the support depends strongly on electrostatic interactions, which are determined by surface charge of the support and the lipid bilayer and by composition and ionic strength of the aqueous environment [38, 39, 46]. In particular, calcium ions have been found to enhance adsorption and rupture of vesicles [38, 40, 44, 46]. The exact mechanism of vesicle rupture is even less understood; most likely it varies depending on the support, the lipids and their interactions [47, 48].

The most common supports for SLBs are mica, glass, silicon and silica [49]. Mica is often regarded as an ideal support, because it exhibits large areas of atomically flat surface. Although large roughness of the surface can prevent formation of continuous bilayers [46, 50], roughness in nm range (such as in the cases of glass and silicon slides) has been shown to have little influence on SLB formation [49, 51]. The bilayer is actually never in direct contact with the support, but it is separated from its surface by a thin aqueous layer (in the order of nanometres), which ensures that fluidity is maintained in SLBs [50, 52, 53]. Nevertheless, lipid mobility is influenced by the proximity of the support and it is slower than in free-standing bilayers [54]. A discussion of the influence of solid

supports on lipid mobility in SLBs is found in section 5.2 of *Attachment I*.

Glass, freshly cleaved mica and silicon slides (which are always covered by a thin layer of silica under ambient conditions [49]) were used as solid supports in the studies presented within this thesis. SLBs were formed by exposing the surface of the solid support to suspension of SUVs prepared by sonication as described in *Attachment IV*. SUVs were used because they had been previously reported to produce defect-free bilayers [39]. Experiments with larger vesicles (prepared by detergent dialysis [55]), yielded also formation of SLBs (see section 2.3); the continuous nature of the resulting SLBs was verified by fluorescence recovery after photobleaching (FRAP) (data not shown).

2. Ellipsometry

2.1. Basic principles of ellipsometry

Ellipsometry is an optical method used mainly for characterization of thin films and surfaces. The method is based on analysis of changes in polarization of light upon its reflection from the sample. Incident beam has an arbitrary elliptical polarization and can be, therefore, described as a superposition of two plane-polarized waves differing, in general, in phase and amplitude. One of the waves in polarized in the plane of incidence defined by the incident and reflected beam (denoted *p*-plane) and the other wave in the plane perpendicular to the plane of incidence (denoted *s*-plane) and, thus, in a plane parallel to the reflecting surface of the sample. Reflection of the two waves from the sample is described by reflection coefficients R_p and R_s respectively. The reflection coefficients are complex numbers; their absolute values give the ratio of the amplitudes of the reflected waves to those of the incident waves; their phases give the phase shifts experienced by the waves upon their reflection. Since R_p and R_s are in general not equal, reflection results in a change of the ratio of amplitudes and mutual phase shift between the waves polarized in *p*- and *s*-plane; therefore, the polarization of the reflected beam differs from the polarization of the incident beam. The change in polarization of light upon reflection can be described by two angles Ψ and Δ, which are the output of an ellipsometric measurement and are related to the complex reflection coefficients by equation (2.1).

$$\rho = \frac{R_p}{R_s} = \tan(\Psi)\exp(i\Delta) \tag{2.1}$$

The ratio ρ of reflection coefficients is determined from the experimentally obtained values of Ψ and Δ and, using an appropriate model, optical parameters of the sample can be inferred from the complex value of ρ [56-58]. In the simplest case, the sample is homogeneous, consisting of a material characterized by complex refractive index n_3 and surrounded by a medium of complex refractive index n_1. Therefore, only reflection on the single interface between the sample and the medium is considered.

Reflection and refraction of electromagnetic waves (polarized in *p*- and *s*-plane respectively) on an interface between two media of complex refractive indices

n_I and n_J is described by Fresnel reflection (r_{pIJ}, r_{sIJ}) and transmission (t_{pIJ}, t_{sIJ}) coefficients (2.2a,b,c,d) [56, 59]:

$$r_{pIJ} = \frac{n_J \cos(\phi_I) - n_I \cos(\phi_J)}{n_J \cos(\phi_I) + n_I \cos(\phi_J)} \tag{2.2a}$$

$$r_{sIJ} = \frac{n_I \cos(\phi_I) - n_J \cos(\phi_J)}{n_I \cos(\phi_I) + n_J \cos(\phi_J)} \tag{2.2b}$$

$$t_{pIJ} = \frac{2\, n_I \cos(\phi_I)}{n_J \cos(\phi_I) + n_I \cos(\phi_J)} \tag{2.2c}$$

$$t_{sIJ} = \frac{2\, n_I \cos(\phi_I)}{n_I \cos(\phi_I) + n_J \cos(\phi_J)} \tag{2.2d}$$

where the angles ϕ_I and ϕ_J are related to each other by Snell's law (2.3).

$$\sin(\phi_J) = \frac{n_I \sin(\phi_I)}{n_J} \tag{2.3}$$

In the simplest case of a single reflecting interface, the reflection coefficients in (2.1) are equal to Fresnel coefficients r_{p13} and r_{s13} (2.2a,b). Substituting (2.2a,b) to (2.1) we arrive to an expression for n_3 (2.4). Refractive index n_3 of the sample can be, then, calculated from the measured values of Ψ and Δ, provided the refractive index n_1 of the medium is known. That is usually the case; the medium is typically air, vacuum or an aqueous solution (transparent in the spectral region used in the ellipsometric experiment) and its refractive index is either known or easily determined by refractometry.

$$n_3 = n_1 \tan(\phi_1)\left[1 - \frac{4\rho \sin^2(\phi_1)}{(\rho+1)^2}\right]^{\frac{1}{2}} \tag{2.4}$$

A typical sample investigated by ellipsometry consists of thin films deposited on a reflecting surface. In the basic case, when only a single layer covers the surface, a three-phase model is used. Parameters of the model are explained in the inset of figure 2.1. The sample is composed of a material with index of refraction n_3 and has a smooth surface on which a layer of thickness d_2 and index of refraction n_2 is deposited. The sample is surrounded by a medium characterized by index of refraction n_1. The angle of incidence ϕ_1 is determined by the arrangement of the ellipsometer and the angle of refraction ϕ_2 can be calculated from Snell's law (2.3).

The reflection coefficient for the wave polarized in q-plane R_q (where the index q stands either for p or s) can be, then, calculated by summation (2.5) of partial waves contributing to the reflected wave [56].

$$R_q = r_{q12} + \sum_{k=1}^{\infty} t_{q12}\, t_{q21}\, r_{q21}^{\,k-1} r_{q23}^{\,k}\, \mathrm{e}^{-i2k\delta} \tag{2.5}$$

where δ is the phase thickness of the thin film (λ is wavelength of the light):

$$\delta = \frac{2\pi\, d_2 n_2 \cos(\phi_2)}{\lambda} \tag{2.6}$$

Summing up the infinite series (2.5) and using identities $r_{q21} = -r_{q12}$ and $t_{q12}\, t_{q21} = 1 - r_{q12}^{\,2}$, the final expression (2.7) for the surface covered by a thin film of optical thickness δ is obtained.

$$R_q = \frac{r_{q12} + r_{q23}\, \mathrm{e}^{-i2\delta}}{1 + r_{q12}\, r_{q23}\, \mathrm{e}^{-i2\delta}} \tag{2.7}$$

The problem of calculating unknown parameters of the sample (refractive indices and film thickness) from the measured values of Ψ and Δ is not trivial and analytical expressions can be found only in few special cases when most of the parameters are *a priori* known [56]. In the case of the three-phase model described above, it is in the situation when all refractive indices are known and the only unknown parameter is, therefore, the film thickness d_2. The analytical formula can be found for example in the monograph of Azzam and Bashara [56]. All other situations require a numerical solution, when estimates of parameters are varied in search for the best agreement between measured values of Ψ and Δ and their estimates calculated using the estimates of unknown parameters.

Measurement of Ψ and Δ at one wavelength λ and one angle of incidence ϕ_1 provides two independent values, from which not more than two unknown parameters can be determined unambiguously. Refractive index n_1 of the medium is typically known (as discussed above) and the refractive index n_3 can be determined using (2.4) from an ellipsometric measurement with the bare substrate (if such sample is experimentally available). Therefore, at least one of the remaining three parameters, which describe the thin film (its thickness d_2 and the real and imaginary part of its refractive index n_2) has to be known in order that the remaining two may be determined in a single spectroscopic measurement. In all ellipsometric

experiments, results of which are presented in this thesis, imaginary part of n_2 was assumed to be equal to 0, because the organic films, investigated here, practically do not absorb light of the visible spectral range (which was used).

If more unknown parameters should be determined by ellipsometry (especially when more complicated models of the sample are used, such as models containing several thin films or models taking into account surface roughness), more experimental data need to be acquired to determine (or overdetermine) all unknown parameters [56]. Typically, measurements are performed for various angles of incidence or various wavelengths of light, which is the principle of variable angle spectroscopic ellipsometry (VASE) [60, 61].

2.2. Practical realization of ellipsometry – Null ellipsometry

Figure 2.1 shows a schematic drawing of an ellipsometric setup. Although it was drawn according to the setup for null ellipsometry used in experiments described in this thesis, most of its parts are valid for any ellipsometric modality. The information on changes in polarization of light upon its reflection from the sample (expressed as ρ) is inferred from the dependence of intensity of light hitting the detector on azimuth angles of the polarizer, analyzer and compensator (an optical element introducing a defined phase shift between waves polarized in two planes perpendicular to each other; it is not necessary in all ellipsometric modalities [56, 60]) and the phase shift introduced by the compensator. The following text will discuss the way of determination of ρ by null ellipsometry, focusing on the particulars which apply to the ellipsometric setup with which data presented in this thesis were obtained.

Null ellipsometry, as its name suggests, searches for such values of adjustable parameters of the instrument, which minimize the intensity of light impinging on the detector, which would reach zero in the ideal case. The typical adjustable parameters in null ellipsometry are the azimuth angles P and A of the polarizer and the analyzer respectively and the azimuth angle C of the compensator fast axis. Adjustment of two parameters is sufficient for reaching the null intensity and one of the three azimuth angles is, therefore, usually fixed [56, 57]. A common null ellipsometer (including the setup used in this work) uses a compensator introducing phase shift $\Delta_C = -\frac{1}{2}\pi$ (quarter-wave plate) to the light polarized in the direction of its slow axis

with respect to the light polarized in the direction of its fast axis. The fast axis of the compensator is fixed at azimuth angle $C = \pm \frac{1}{4}\pi$, using the usual notation according to which all azimuth angles are measured anti-clockwise from the plane of incidence when looking against the propagating beam [57].

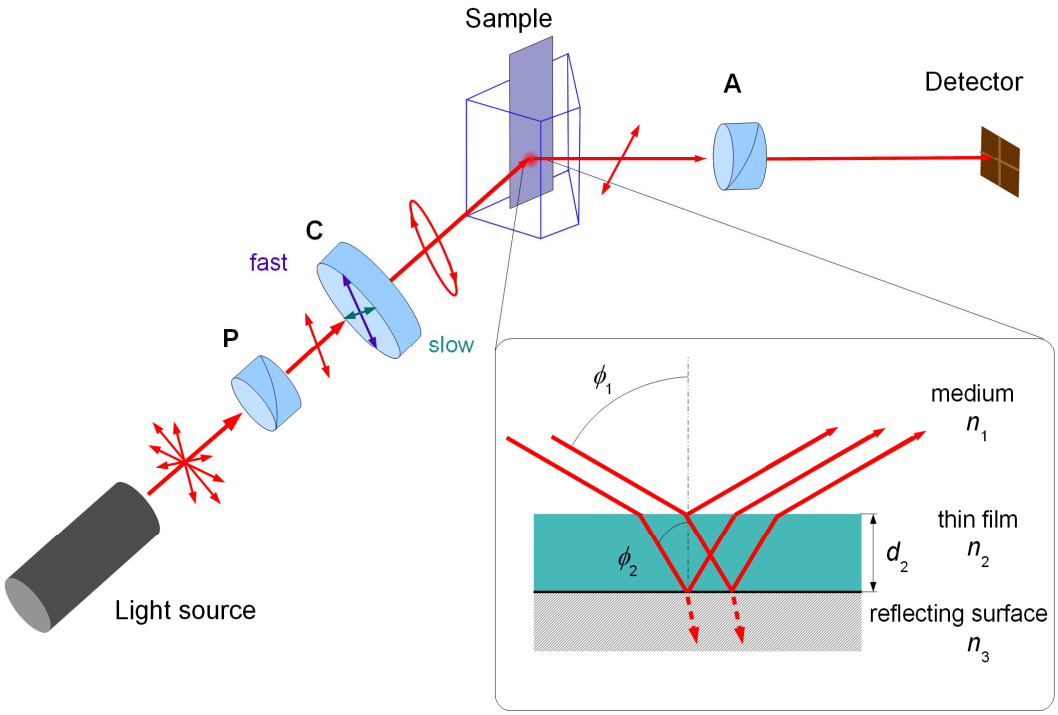

Figure 2.1: Schematic drawing of a null ellipsometer. A light source (a laser in the setup described in this thesis) produces randomly (or circularly) polarized light, from which polarizer (**P**) selects a plane-polarized wave. Depending on the orientation of its polarization with respect to the fast and slow axis of the compensator (**C**) (a quarter-wave plate in the described setup), an arbitrary elliptically polarized light is produced, which impinges on the sample. Such orientation of polarizer can be found, for which the light reflected from the sample is plane-polarized. Orientation of its polarization is determined by searching for the orientation of analyzer (**A**), which gives the minimum of intensity on the detector. The inset shows the three-phase model of the sample consisting of a reflecting surface characterised by refractive index n_3, a thin film of thickness d_2 and refractive index n_2 and a medium of refractive index n_1.

The compensator changes linearly polarized light to elliptically polarized

light; arbitrary ellipticity can be achieved by adjusting the azimuth angle *P*. For certain values of ellipticity and orientation of the ellipse, the reflected light is linearly polarized. In such cases, null intensity on the detector is reached by setting the azimuth angle *A* perpendicular to the plane of polarization of the reflected light. If the azimuth angles *A* and *P* are searched within the range $\langle 0; 2\pi \rangle$, eight combinations of *A* and *P*, minimizing detected intensity (to null in ideal case), can be found for each of the two compensator azimuth angles $C = \pm \frac{1}{4}\pi$. It can be shown that, without any loss of generality, the range within which *A* and *P* are searched can be reduced to $0 < A \leq \frac{1}{4}\pi$ and $-\frac{1}{4}\pi \leq P < \frac{3}{4}\pi$ respectively [57]. Then, in the case of reflection from a sample characterized by reflection coefficients ratio ρ (2.1), the angles A_0 and P_0 corresponding to minimal (null) intensity are related to Ψ and Δ by relations (2.8a,b) when $C = \pm \frac{1}{4}\pi$.

$$\Psi = A_0 \tag{2.8a}$$

$$\Delta = \pi \pm \frac{\pi}{2} \mp 2P_0 \tag{2.8b}$$

The condition of null intensity is also satisfied for $A = A_0 + k\pi$ and $P = P_0 = \frac{k}{2}\pi$, where *k* is an integer, giving the eight combinations for each value of *C*. Derivation of relations (2.8a,b) using the Jones matrix formalism can be found for example in [56].

Ellipsometric measurements presented in this thesis were performed with a modified Rudolph & Sons ellipsometer Type 43303-200 E [58, 62]. A He-Ne laser (λ = 632.8 nm) was used as the light source ensuring good stability and high signal to noise ratio [62]. The polarizer and analyzer are rotated by stepper motors with accuracy and reproducibility within 0.005º, which allows determination of layer thicknesses with precision of approximately 0.5 nm [62]. Measurements with surfaces immersed into liquid are enabled by placing the reflecting surface to a cuvette of trapezoidal cross-section which ensures perpendicular incidence of light at the cuvette walls. A magnetic stirrer placed bellow the cuvette allows stirring of the liquid with defined velocity.

The angle of incidence is set to 68º, which was found to be ideal for ellipsometric measurements on silicon surfaces (W. Th. Hermens, personal

communication). The sensitivity of ellipsometric measurements is, in general, the highest at incidence angles close to the principal angle for the given interface. The principal angle is the angle of incidence at which the difference between phase shifts δ_p and δ_s experienced by *p*- and *s*-polarized planes respectively upon their reflection is equal to $\frac{1}{2}\pi$. In the case of reflection from materials with low extinction coefficient, principal angle is almost identical with Brewster angle, at which only *s*-polarized wave is reflected [56, 59]. For silicon (covered with thin layer of SiO_2) in air, the principal angle is approximately 70º. However, the experimental scatter in measured angle Ψ and Δ increases with increasing sensitivity and errors in determination of Δ increase significantly with increasing angle of incidence [56]. Therefore the angle of 68º was chosen as a compromise between requirements on sensitivity on one hand and on precision and accuracy on the other hand.

The set of azimuth angles satisfying the nulling condition can be found in two steps: first the polarizer is adjusted to minimum intensity and, then, the null is found by adjustment of the analyzer [56]. To achieve higher precision, intensity can be minimized by alternating adjustments of *P* and *A* until it cannot be reduced any further. If a temporal sequence of measurements with the same sample is performed (for example to follow kinetics of adsorption processes on the surface), the time needed for minimum intensity search can be reduced by searching only in the vicinity of P_0 and A_0 found in the preceding measurement, provided the changes in optical parameters between two readings are small enough. In this way, the ellipsometer used in this work can perform a new reading every 12 – 15 s. Further increase in temporal resolution can be achieved by searching for intensity minimum via polarizer adjustments only (off-null ellipsometry [63]); such approach was however not needed to follow processes investigated in this work.

2.3. Lipid bilayers characterized by ellipsometry

Thanks to its ability to reach sub-nanometre resolution in layer thickness (d_2), ellipsometry allows measurement of SLB thickness and its changes during SLB formation or its interaction with other molecules. The above described three-phase model is applicable also in this case: reflecting surface (n_3) is formed by the solid support; fully hydrated SLB (a mixture of phospholipids and aqueous solution) represents the thin film (n_2, d_2) and the whole sample is in an aqueous solution (n_1).

Lipids and most peptides and proteins do not absorb light in the visible spectral range. Therefore, imaginary part of n_2 can be assumed equal to 0 and the remaining parameters describing the layer (real part of n_2 and d_2) can be determined unambiguously from measured Ψ and Δ. When the chemical composition of the adsorbed layer is known, its surface mass Γ (mass per unit area) can be determined from n_2 and d_2 using molar refractivity of its constituents. When the Lorentz-Lorenz theory for refractive index of a mixture of substances [59] is used, equation (2.9) for Γ of a mixture of lipids (or lipids and proteins) and buffer is derived [58, 64].

$$\Gamma = d_2 \left(\frac{L(n_2) - L(n_1)}{\frac{A}{M} - v\,L(n_1)} \right) \tag{2.9}$$

where A, M and v are molar refractivity, molar mass and partial specific volume respectively of the lipid (or lipids and proteins) mixture forming the adsorbed layer. L (n_I) is defined by (2.10).

$$L(n_I) = \frac{n_I^{\,2} - 1}{n_I^{\,2} + 2} \tag{2.10}$$

Molar refractivity of different compounds can be calculated using molar refractivity of atoms or atom groups. Partial specific volume of different lipid mixtures was determined by Cuypers et al. [58] from ellipsometric measurements of thickness of dry lipid films (see the reference for details on the method and further discussion). The following values were used in the studies presented here (*Attachment II* and *Attachment III*): A/M = 0.274 cm^3g^{-1} and v = 0.89 cm^3g^{-1}.

Figure 2.2 shows an example of SLB formation on different solid supports monitored by ellipsometry. It is evident from the figure that, in all three cases, vesicles first adsorb to the solid support without rupturing (high thickness d_2 and low refractive index n_2 which is only slightly higher than refractive index of the buffer n_1 = 1.335) and, only after a certain critical coverage has been reached, the vesicles rupture and coalesce into a bilayer (see section 1.3 for more information on SLB formation). The gradual decrease in thickness of the layer on silicon slide during the first 100 s of the measurement is probably caused by flattening of the vesicles on the surface.

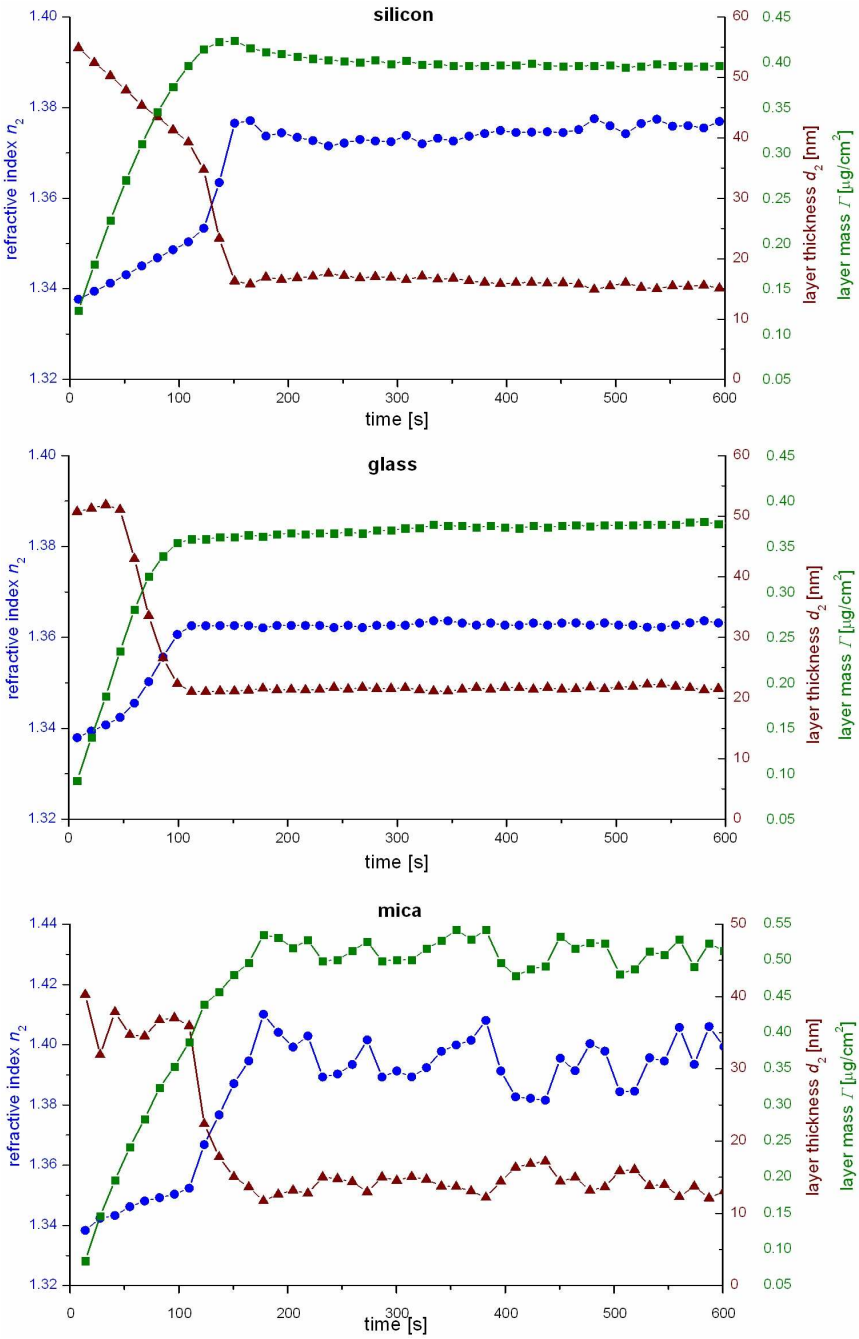

Figure 2.2: Formation of SLBs by adsorption and rupture of vesicles on three different solid supports (silicon slides, glass and freshly cleaved mica) monitored by ellipsometry. Refractive index n_2 (circles), thickness d_2 (triangles) and layer mass Γ (squares) are plotted versus time form the addition of vesicles to the sample. The vesicles were prepared of dioleoyl-phosphatidylcholine (DOPC) and dioleoyl-phosphatidylserine (DOPS) in molar ratio 4/1 by octyl glucoside dialysis [55]; SLBs formed in a buffer composed of 10 mM 4-(2-hydroxyethyl)-1-piperazineethanesulfonic acid (HEPES), 150 mM NaCl, 2 mM $CaCl_2$ (pH 7.4); the lipid concentration in

the sample was 100 μM.

Formation of SLBs on the same three solid supports has been studied in detail by Beneš et al. [44]. The authors observed trends similar to those presented in figure 2.2; slight differences are possibly caused by different vesicle preparation protocol (resulting in different size distribution of vesicles) used in [44] and in the experiment described here. Beneš et al. also reported need for high critical coverage (more 50 % of bilayer mass) for SLB formation on silicon slides and on mica. SLB formation on glass was dominated by direct vesicle-support interactions and direct rupture of vesicles was observed under some conditions. That correlates with the presented results, according to which the critical coverage needed for SLB formation on glass was the lowest from all the studied supports, as can be seen from the fraction of total layer mass Γ at which rupture started (figure 2.2). The adsorption of vesicles on mica was slightly slower than on other supports, which agrees with [44]. Furthermore, the speed of SLB formation on all supports depended on concentration of vesicles in the sample; two times lower lipid concentration (50 μM) resulted in approximately two times longer time required to reach the full mass of the adsorbed layer (data not shown).

It can be also noted that the scatter in calculated values of n_2 and d_2 of the SLB on mica is relatively high and also that the scatter is covariant (overestimation of n_2 results in underestimation of d_2 and *vice versa*). Therefore the scatter in layer mass Γ is much smaller and Γ is the most robust parameter obtained from ellipsometric measurements and it can be measured for lipid bilayers with a precision of 2–4 ng/cm^2 [44, 58]. The approximate value of $\Gamma = 0.4$ μg/cm^2 obtained in the presented experiment corresponds to area per lipid (using the average molecular mass of a lipid in the used mixture) equal to $S_0 = 0.66$ nm^2, which is in good agreement with findings of X-ray structure analysis [65, 66].

The measured value of d_2 (figure 2.2) is considerably higher than the expected thickness of a lipid bilayer (which is approximately 5 nm including the thin aqueous layer separating the bilayer from the solid support [67-73]). The systematic overestimation of d_2 (and most likely simultaneous underestimation of n_2) is probably caused by surface roughness, which is not considered in the three-phase model, and also by imperfections of optical components of the ellipsometer [44, 74].

This type of systematic error, however, affects only the absolute values of d_2 and n_2; the observed trends, such as vesicle rupture after reaching a critical coverage, are not invalidated by it. Our measurement of SLB formation on a silicon slide performed with a spectroscopic ellipsometer and analyzed using a four-phase model (taking into account the thin layer of silica which is present on the surface of silicon at ambient conditions) yielded more realistic values of d_2 (5–10 nm) [75].

In some ellipsometric studies of SLBs, a constant value of refractive index n_2 is used (for example 1.45 [76, 77]) and the thickness of the bilayer d_2 is the only free parameter calculated from Ψ and Δ [76-80]. By proper choice of n_2, a good agreement of measured d_2 with expected value can be reached. However, processes involving changes in density of the layer (which is influencing the refractive index) cannot be monitored by such approach. The independent determination of n_2 and d_2 is necessary to distinguish the critical coverage step in SLB formation (as shown in figure 2.2). It is also essential for elucidating mechanisms of SLB degradation. For example in the case of phospholipase A2 a loss in surface mass Γ was accompanied by decrease in n_2 and a constant thickness d_2, showing that phospholipase A2 is removing the bilayer in patches, which are separated by remaining parts of intact SLB [44]. If constant value of n_2 was used, the process could be misinterpreted as bilayer thinning. Similar situations are encountered in interpretation of effects of AMPs on lipid bilayers (*Attachment II* and *Attachment III*).

3. Atomic force microscopy

Atomic force microscopy (AFM) is one of the techniques of scanning probe microscopy. It probes the topography of surfaces with resolution on nanometre (or even sub-nanometre) scale by a small pyramidal-shaped probe (the tip) located at the end of an elastic cantilever (usually made of silicon or silicon nitride) [49]. The principle of the method is schematically depicted in figure 3.1. The sample is moved with respect to the tip by a piezoelectric actuator; the forces between the tip and the sample surface (dominated typically by attractive van der Waals forces and repulsive forces between electrons of atoms at the tip and molecules at the surface) are monitored via changes in deflection or oscillation of the cantilever [81, 82]. Information on tip-surface forces is used to construct a map of topography of the sample surface; alternatively other characteristics, such as viscoelasticity [83, 84] or localization of specific molecules (when using a chemically functionalized tip [85, 86]), can be also mapped.

There exist several modes of AFM operation, which differ in the range of accessible characteristics of the sample and in the way how the tip-sample forces are monitored. In contact mode, the tip is kept in contact with the scanned surface. Deflection of the cantilever is determined by equilibrium between tip-surface attractive and repulsive forces and spring force of the elastic cantilever [49, 81, 82]. Changes in tip-surface distance and, thus, in tip-surface forces, are accompanied by changes in cantilever deflection (which is monitored via movements of the laser beam reflected from the upper side of the cantilever; see figure 3.1). A constant deflection of the cantilever (and, thus, constant tip-surface force) is maintained throughout the whole scan by adjusting the vertical position of the sample (the *Z*-coordinate of the piezoelectric actuator). The *Z*-coordinates corresponding to individual points in the plane of the scan (*XY*-plane) represent, then, the topographic image of the sample surface (provided that the dependence of tip-surface force on tip-surface distance is uniform in the *XY*-plane).

Tapping mode (or intermittent contact mode) was developed later with the aim of minimizing lateral forces, which the tip exerts on the sample [83, 85, 87]. That is important especially for imaging soft surfaces of biological samples, which can be considerably affected by lateral tip-sample forces. In tapping mode, the

cantilever is oscillated at a frequency close to its resonance frequency and the amplitude of the oscillation is monitored. Tip-surface forces influence the cantilever oscillation and reduce its amplitude at shorter tip-surface distances. Therefore, by adjusting the *Z*-position of the sample to keep constant amplitude of cantilever oscillation, the topography of the sample surface is obtained [49, 83, 87].

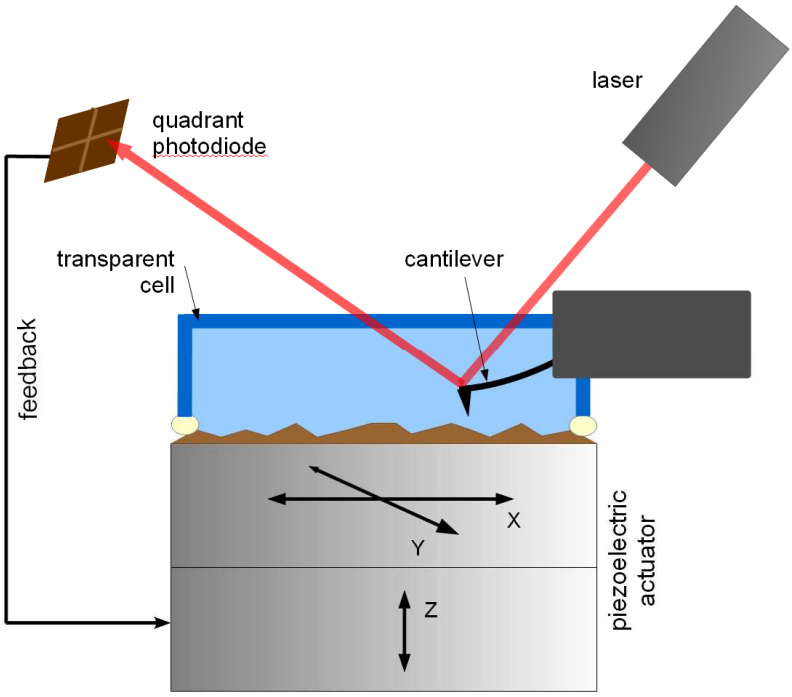

Figure 3.1: Schematic depiction of AFM setup for imaging in aqueous environment (the sample is placed in a transparent cell filled with desired solution). The piezoelectric actuator moves the sample with respect to the cantilever, movements of which are monitored via a laser beam reflected from its upper side (opposite to the tip). Laser beam impinges upon a quadrant photodiode and, according to the ratio of intensities in individual quadrants, vertical (*Z*) sample position is adjusted to maintain constant cantilever deflection or oscillation amplitude (in tapping mode).

The topography of planar surfaces without any distinct morphological features (such as homogeneous SLBs or their solid supports) can be sufficiently characterized in terms of surface roughness. A commonly used roughness characteristic, which is often extracted from AFM images, is root-mean-square roughness R_q defined by equation (3.1), where M is the number of points in the scan and Z_m is their average Z-coordinate [88].

$$R_q = \left[\sum_{k=1}^{M} \frac{(Z_k - Z_m)^2}{M} \right]^{\frac{1}{2}} \quad (3.1)$$

One of the main advantages of AFM is its ability to image surfaces in aqueous environment. It allows, therefore, recording of high-resolution images of biological samples, including living cells, under physiological conditions [89-92]. SLBs are, thanks to their planar character, well suited for investigation by AFM. Indeed, AFM is an indispensable source of information on SLB thickness [69, 93-95], phase separation in lipid bilayers [70, 96] or pathways of SLB formation [38, 40, 49]. Interaction of proteins and peptides with lipid bilayers is also frequently investigated by AFM [67, 84, 97-99]; however, in the studies presented in this thesis, AFM played only a marginal role. It will be therefore not discussed any further here; results of AFM experiments are presented in section 5.2.

4. Confocal fluorescence microscopy

4.1. Laser scanning microscopy

Confocal fluorescence microscopy is a widely used imaging technique in biological sciences. Its development was motivated mainly by efforts to improve contrast in imaging of thick biological samples by fluorescence microscopy, in which case fluorescence originating elsewhere than in the focal plane of the microscope contributed to the image in the form of a blurred background [100, 101]. The cost for rejecting out-of-focus light is the impossibility of capturing the whole image at once and the need to record it point-by-point instead. That fact imposes limits on image acquisition speed but, on the other hand, allows further analysis of fluorescence signal originating from individual points in the sample. Therefore, a confocal florescence microscope has much broader application than just imaging of thick samples.

The basic setup of a typical confocal fluorescence microscope is shown in figure 4.1. Excitation light (typically a collimated laser beam) is coupled by a dichroic mirror reflective at the wavelength of the laser and transmissive at longer wavelengths, where fluorescence emission of the sample is located, into the objective, which focuses the light into a small volume element within the sample. Fluorescence emission is collected by the same objective; passes the dichroic mirror and emission filter (which eliminates the rest of the excitation light transmitted through the dichroic mirror) and is again focused by tube lens onto a small circular aperture (usually of a diameter in the range from 30 to 100 μm) called confocal pinhole. Positioning of the pinhole to tube lens back focal plane ensures that fluorescence originating from the focal plane is focused at the plane of the pinhole and, therefore, propagates through the aperture, while further propagation of out-of-focus fluorescence (which is unfocused at the pinhole plane) is, to a large extent, stopped. Light that passes through the pinhole reaches a detector, which is usually a single photon avalanche diode or a photomultiplier tube.

The above described setup ensures that fluorescence emission is effectively collected only from a small volume element of the sample, the detection volume of the confocal microscope, which determines resolution in confocal microscopy. It is the product of distribution of excitation light intensity within the sample and of the

collection efficiency of emitted fluorescence. The distribution of excitation light depends on the objective numerical aperture, which determines the smallest possible size of a focused beam via the diffraction limit. Fluorescence collection efficiency is also determined by the objective numerical aperture and by the pinhole size and positioning. The resulting diffraction limited effective detection volume has typically about 1 μm^3 or less [102, 103].

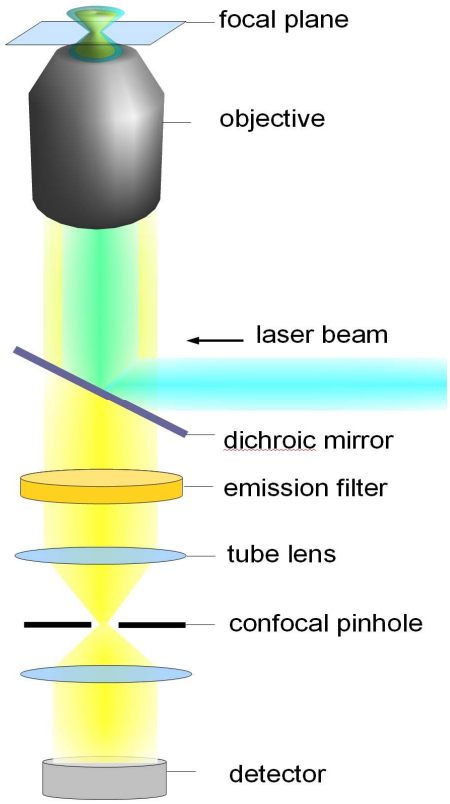

Figure 4.1: Basic setup of a confocal fluorescence microscope. Excitation light (a collimated laser beam) is reflected by a dichroic mirror to the objective, which focuses the light to a small volume element within the sample. Fluorescence from the sample is collected by the same objective, transmitted by the dichroic mirror and emission filter and focused by tube lens to the confocal pinhole, which prevents out-of-focus fluorescence from reaching the detector.

The excitation laser beam has typically a Gaussian intensity profile (corresponding to the basic transverse electromagnetic TEM_{00} mode of the laser) producing a Gaussian intensity profile of the focus in planes parallel to the focal plane (*XY*-planes), which gives rise to Gaussian distribution of collected fluorescence intensity [104-106]. The intensity profile of detected fluorescence in axial direction (*Z*-axis; the direction parallel to the optical axis of the microscope) can be approximated by a Lorentzian function [105, 107, 108], resulting in formula (4.1) giving Gaussian-Lorentzian spatial distribution $W_{GL}(R,Z)$ of probability of detecting a photon from a molecule at coordinates *R* and *Z*.

$$W_{GL}(R,Z) = \frac{\omega_0^{\,2}}{\omega^2(Z)} \exp\left(-2\,\frac{R^2}{\omega^2(Z)}\right) \tag{4.1}$$

where $R^2 = (X^2 + Y^2)$ and $\omega(Z)$ is defined by equation (4.2) and describes width of the detection volume at a plane characterised by axial coordinate Z [106, 109].

$$\omega^2(Z) = \omega_0^{\,2}\left(1 + \frac{\lambda^2 Z^2}{\pi^2 \omega_0^{\,4}}\right) \tag{4.2}$$

ω_0 is a characteristic dimension of the detection volume in the focal plane ($Z = 0$). Its size is diffraction limited and usually in the range from 200 to 500 nm, depending on the objective numerical aperture and wavelength λ of excitation light in the medium of the sample [102, 110]. The detection volume is often described by a 3-dimensional Gaussian shape $W_G(R,Z)$ (4.3), especially in situations when integration over the detection volume is performed. The axial intensity profile is, then, approximated by a Gaussian function analogous to the intensity profile in the focal plane, in which ω_0 is replaced by ω_Z, a characteristic dimension of the detection volume in the axial direction, which is usually 4 to 8 times larger than ω_0 [102, 110].

$$W_G(R,Z) = \exp\left(-2\,\frac{R^2}{\omega_0^{\,2}}\right)\exp\left(-2\,\frac{Z^2}{\omega_Z^{\,2}}\right) \tag{4.3}$$

Several more complex models have been proposed, which describe the real profile $W(R,Z)$ of the detection volume more closely [111-114]. The influence of optical aberrations and microscope misalignment on the shape and dimensions of the detection volume was studied extensively by Jörg Enderlein and his coworkers [102, 103].

The image is formed by scanning the sample with the detection volume and, thus, collecting emission from different locations within the sample. Therefore, imaging with the above described confocal setup using laser excitation is frequently called laser scanning microscopy (LSM) and the term will be used also in the following text. The point-wise image formation imposes limitations on image acquisition speed in LSM. On the other hand, it allows independent analysis of fluorescence characteristic such as emission spectra or fluorescence lifetime in individual points of the sample.

There exist two main methods of scanning the sample with the detection

volume in LSM [100, 115, 116]. Beam scanning is based on deflecting the optical path of the laser beam entering the objective; a pair of mirrors oscillated by a galvanometer is commonly used for that purpose. The position of the detection volume is, thus, moved to different points in the *XY*-plane; scanning in *Z*-direction is usually achieved by axial positioning of the objective. Sample scanning moves the sample stage with respect a stationary excitation beam. Movements of the stage in all three dimensions are usually realized by a piezoelectric actuator. Equivalently, a stationary sample stage together with a stationary excitation laser beam may be used, when the objective is moved. The last option (with the objective moved in all three directions by a piezoelectric actuator) was applied in the LSM setup with which data presented in this thesis were acquired. Beam scanning is typically much faster in the *XY*-plane than stage or objective scanning. However, speed of image acquisition was not crucial in experiments described here, because the investigated samples (SLBs) are stable and not moving on time-scales much longer than times needed for image acquisition. Slow scanning with longer acquisition time in each point was preferentially used in order to obtain more accurate information on fluorescence intensity distribution suitable for further quantitative analysis. The objective scanning setup also allows positioning of the detection volume into any selected point of the sample for performing longer measurements such as those of fluorescence correlation spectroscopy (FCS) explained in section 4.3.

To reach the maximal possible resolution, which is limited by the size of the effective detection volume, signal from each point of the sample has to be collected and, therefore, focus has to be moved in steps smaller than the characteristic dimension of the detection volume in the respective direction [117, 118]. Several special techniques have been developed to enhance resolution in confocal microscopy beyond the diffraction limit (typically by exploiting non-linear optical phenomena). Probably the best known among them is stimulated emission depletion (STED) microscopy [119-123]. Another technique called dynamic saturation optical microscopy (DSOM) can be implemented in most laser scanning microscopes in a straightforward manner and has the advantage of not requiring neither complex optical setup nor advanced numerical image processing. It requires, however, fluorophores of rather high photostability and long dwelling time in a dark state (such as triplet state) [105, 124, 125].

4.2. LSM of supported lipid bilayers

In order to be visualized by LSM, SLBs need to be fluorescently labelled. They are usually prepared from a mixture of lipids containing fluorescently labelled lipids or lipophilic fluorescent probes, often structurally resembling phospholipids in order to be incorporated into the lipid bilayers in a well defined manner (examples of such probes are given in section 5.4 of *Attachment I*). Phospholipids labelled with BODIPY dyes were predominantly used in this work, because of the relatively high photostability and low environmental sensitivity of the dye [126].

The SLB sample for LSM imaging should be positioned in the focal plane of the microscope and immersed in an aqueous solution to maintain its hydration. A cuvette for microscopy of SLBs was described by Benda et al. [127, 128]. The solid support is fixed to a holder and immersed in an aqueous solution in the cuvette; the surface with the SLB is facing downwards (towards the objective) and is aligned perpendicular to the optical axes of the microscope within a short distance (less than the working distance of the objective) above the bottom of the cuvette, which is made of a cover-slip. SLBs on any support, including non-transparent surfaces like silicon, can be imaged in such cuvette. Transparent solid supports such as glass or mica are common in microscopy of SLBs, allowing a much simpler arrangement to be used. The SLB is illuminated through the transparent solid support, which either forms the bottom of a cuvette or a drop of aqueous solution is deposited on the surface of the support. Correction ring of the objective has to be adjusted to compensate for the thickness and refractive index of the solid support, when it is placed within the optical path of the beam.

A sample (or objective) scanning system allows recording of scans in any plane perpendicular to one of the axes *X*, *Y*, *Z*. *XY*-scans of SLBs display usually a homogeneous distribution of intensity; only relatively large defects (comparable or larger than ω_0) can be visualized. *XZ*-scans show the axial profile of the detection volume $W(Z)$ (see figure 1 in *Attachment II* or figure 2 in *Attachment III*) and provide no information on the bilayer thickness, which is approximately 3 orders of magnitude smaller than ω_Z (and, thus, the axial resolution). *XZ*-scans are, however, very useful when quantitative conclusions are drawn from intensity changes in LSM images. The intensity of *XY*-scans depends strongly on the mutual position of the focal plane and the plane of the SLB; a small displacement of the SLB from the focal

plane can cause significant decrease in intensity.

Fluorescent molecules are mobile in SLBs and there is a constant exchange of molecules within the detection volume, which reduces the risk of artefacts due to photobleaching. For that reason SLBs were chosen as a convenient system for testing the axial resolution of DSOM (they are not suitable for testing the lateral resolution, because of the homogeneous intensity distribution in *XY*-scans). The resolution achieved by DSOM was found to be 4 times better than in standard LSM [105].

4.3. Principles of fluorescence correlation spectroscopy

Fluorescence correlation spectroscopy was developed in 1970s [129-131] and since then has become a widespread method for measuring translational and rotational diffusion coefficients or flow velocities of fluorophores or fluorescently labelled molecules, kinetic rate constants of chemical reactions, critical micelle concentrations and other quantities, which can be related to fluctuations in observed fluorescence intensity [104]. Nevertheless, characterization of molecular translational diffusion has been probably always the most common and best established application of FCS. The spread of FCS is closely connected with the advances in instrumentation, especially in confocal microscopes, which are the most common instruments for FCS. Therefore, combination of FCS with LSM imaging is straightforward and widespread, above all in biological applications of FCS.

The standard confocal FCS method is based on statistical analysis of temporal fluctuations of fluorescence intensity originating from the detection volume of a confocal microscope. The principle of the method is schematically depicted in figure 4.2. The autocorrelation function $G(\tau)$ defined by equation (4.4) is calculated from the time-trace of fluorescence intensity $I(t)$ either by a hardware correlator or by software processing; the latter being more versatile and preferred nowadays [132]. The pointed brackets in equation (4.4) signify temporal averaging.

$$G(\tau) = \frac{\langle I(t)\, I(t+\tau)\rangle}{\langle I(t)\rangle^2} \tag{4.4}$$

The shape of the autocorrelation function $G(\tau)$ contains information on the time-scale of processes underlying the observed intensity fluctuations. It rises steeply to its maximum value on nanosecond time-scale; the effect (photon antibunching) is

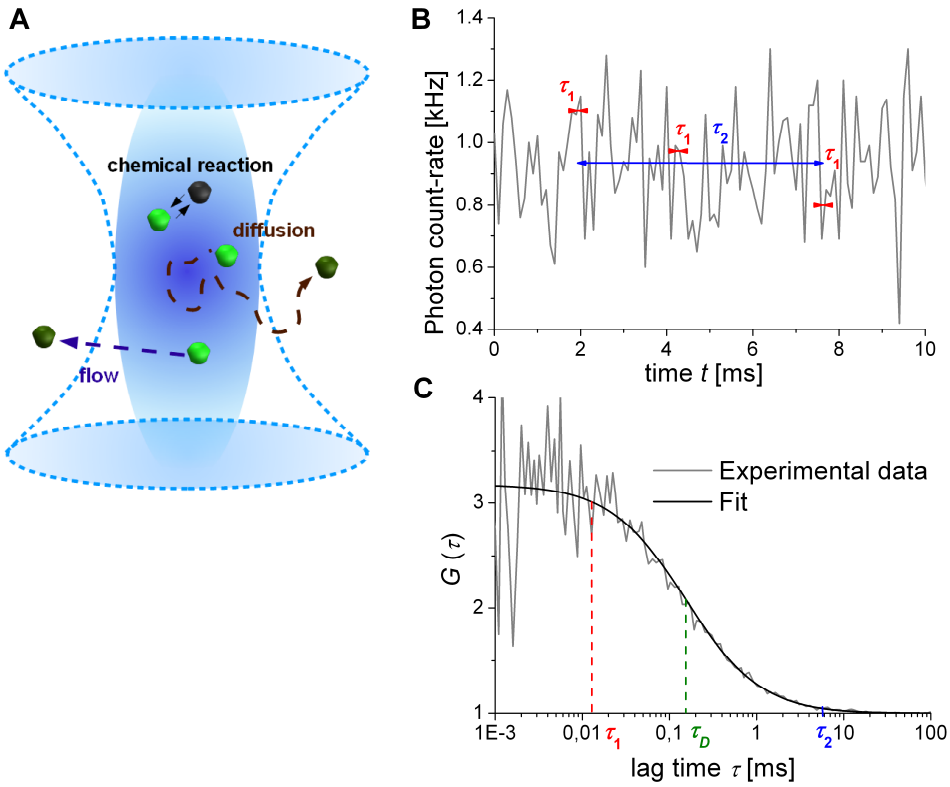

Figure 4.2: Basic principles of confocal FCS. Fluorescence is collected from the detection volume of a confocal microscope; the observed fluctuations of its intensity are typically caused by diffusion or flow of fluorescent particles or by chemical reactions accompanied by changes in brightness of the fluorophore (**A**). In the case of an aqueous solution of a fluorophore, the fluctuations on ms time-scale result from diffusion of fluorophore molecules in and out of the detection volume (**B**). For a short lag time τ, the probability is high that a molecule is in the detection volume at time $t + \tau$ if it was there at time t. That results in a high value of the autocorrelation $G(\tau)$. For longer lag times τ, the fluctuations become random and $G(\tau)$ approaches its asymptotic value $G(\infty)$. The characteristic diffusion time τ_D a molecule spends diffusing through the detection volume corresponds to the value of $G(\tau)$ equal to the average of its maximum $G(0)$ and its minimum $G(\infty)$ (**C**).

related to the minimal time delay between two photons emitted by a single fluorophore and, thus, to the lifetime of fluorescence and number of individual fluorophores within the detection volume [133, 134]. Decay of $G(\tau)$ on microsecond time-scale results from fluctuations caused mainly by photophysical and photochemical processes (such as intersystem crossing to non-fluorescent triplet state

or excited state reactions) and rotational diffusion of molecules (in the case of polarized detection). Decay on longer time-scales is related to translational diffusion of molecules in and out of the detection volume (which is the process most frequently addressed by FCS) or chemical reactions associated with a change in brightness (photon count-rate per molecule) of the fluorophore. If more processes happen on the same time-scale, their contributions to $G(\tau)$ are not easy to separate. Time-scales shorter than microseconds are not accessible in most FCS experiments and therefore only the decay of $G(\tau)$ is usually analysed [102, 103, 135, 136].

More detailed information on processes underlying the fluorescence intensity fluctuations can be extracted from fitting the experimentally obtained autocorrelation function with a theoretically derived model. Let us assume that the sample is a solution containing fluorophores of brightness Q (photon count-rate per molecule when the fluorophore is located in the centre of the detection volume) in concentration C. The measured fluorescence intensity is, then, given by (4.5)

$$I(t) = \int_V W(\mathbf{R})\, Q\, C(\mathbf{R},t)\, \mathrm{d}V \tag{4.5}$$

If the brightness Q is constant in time, fluctuations in fluorescence intensity are caused by fluctuations in concentration $C(\mathbf{R},t)$ solely. The shape of the autocorrelation function $G(\tau)$ is, therefore determined by term $\langle C(\mathbf{R},t)\, C(\mathbf{R}',t+\tau)\rangle$, which, in the case of free diffusion characterized by diffusion coefficient D, can be expressed by following relation [129, 134, 137]:

$$\langle C(\mathbf{R},t)\, C(\mathbf{R}',t+\tau)\rangle = \langle C(\mathbf{R},0)\, C(\mathbf{R}',\tau)\rangle = \frac{\langle C\rangle}{(4\pi D\tau)^{-3/2}} \exp\left(-\frac{(\mathbf{R}-\mathbf{R}')^2}{4D\tau}\right) \tag{4.6}$$

The autocorrelation function (4.7) is, then, calculated by substituting (4.5) and (4.6) into (4.4).

$$G(\tau) = 1 + \frac{1}{N}\frac{1}{1+(\tau/\tau_D)}\left(\sqrt{\frac{1}{1+(\tau/\tau_D)(\omega_0/\omega_Z)^2}}\right) \tag{4.7}$$

where $N = \langle C\rangle V_{eff}$ is the average number of independently diffusing fluorescent particles (either individual fluorophores or supramolecular structures containing more fluorophores such as micelles or liposomes) in the effective detection volume V_{eff}, which is defined by (4.8) for a 3-dimesional Gaussian profile (4.3) [138].

$$V_{eff} = \frac{\left(\int_V W_G(\mathbf{R})\,\mathrm{d}V\right)^2}{\int_V {W_G}^2(\mathbf{R})\,\mathrm{d}V} = \pi^{\frac{3}{2}}\,\omega_0\,\omega_Z \tag{4.8}$$

τ_D is called diffusion time and it is the time a fluorescent particle spends on average within the detection volume. It is related to diffusion coefficient D by (4.9) [104, 139].

$$\tau_D = \frac{{\omega_0}^2}{4D} \tag{4.9}$$

It is obvious from equations (4.8) and (4.9) that by fitting the measured autocorrelation function with model (4.7), diffusion coefficient D and concentration C of fluorescent particles can be determined, provided the dimensions of the detection volume are known. A calibration FCS measurement in a solution of a standard florescent dye with precisely known diffusion coefficient is usually performed to determine detection volume dimensions [140].

If the transition of fluorophores to a nonfluorescent triplet state cannot be neglected, it is described by an exponential term introduced to (4.7), where T is the fraction of fluorophores in triplet state and τ_T is intersystem crossing relaxation time [135].

$$G(\tau) = 1 + \left[1 - T + T\exp\left(-\frac{\tau}{\tau_T}\right)\right]\frac{1}{N(1-T)}\frac{1}{1+(\tau/\tau_D)}\sqrt{\left(\frac{1}{1+(\tau/\tau_D)(\omega_0/\omega_Z)^2}\right)} \tag{4.10}$$

If the sample contains M populations of fluorescent particles with different diffusion times τ_{Dk}, a more general model (4.11) is needed. The contribution of each population is weighted by the fraction F_k of the overall number of fluorescent particles N it represents and by the square of its brightness Q_k [104, 141].

$$G_M(\tau) = 1 + \frac{\sum_{k=1}^{M}(Q_k)^2 F_k g_k(\tau)}{N\left(\sum_{k=1}^{M} Q_k F_k\right)^2}, \quad g_k(\tau) = \frac{1}{1+(\tau/\tau_{Dk})}\sqrt{\frac{1}{1+(\tau/\tau_{Dk})(\omega_0/\omega_Z)^2}} \tag{4.11}$$

The exponential decay describing transition of fluorophores to triplet state can be introduced to $g_k(\tau)$ in a manner analogous to its introduction to (4.7) resulting in (4.10).

4.4. Practical aspects and artefacts of FCS

The signal-to-noise ratio in FCS is the highest when there is on average approximately one fluorescent particle in the detection volume [127, 142]. This means that very low concentrations (usually in the nM range) of fluorescent particles are ideal and, therefore, FCS is sometimes considered a single-molecule technique, although the autocorrelation curve always contains averaged contributions from a large number of molecules [143-145]. Analysis of accuracy of concentration and diffusion time determination represents a nontrivial problem, because of highly non-linear relation of C and D to the measured fluorescence fluctuations [110, 146]. Several methods have been developed for that purpose [132, 146, 147]; errors of FCS results presented in this thesis were estimated by the method of Wohland et al. [127, 132].

Systematic errors in FCS can be caused by deviations of the real detection volume shape from the 3-dimensional Gaussian profile (4.3) assumed in equations (4.8) and (4.9) [112]. Such deviations are enhanced by optical aberrations of the laser beam, misalignment of confocal pinhole position, refractive index mismatch between immersion liquid and the sample and by photobleaching and optical saturation (nonlinearity in dependence of fluorescence intensity on excitation intensity resulting from depletion of ground-state fluorophore population caused by high excitation rate) [102, 103, 148]. The optimal excitation intensity in FCS is, therefore, a compromise between the requirement of high number of fluorescence photons needed for statistical accuracy of the autocorrelation function (a tenfold reduction of excitation intensity means approximately a hundred times longer measurement to reach a comparable statistical accuracy [142, 148, 149]) and the need to minimize photobleaching and saturation artefacts. The maximal excitation intensity at which no photobleaching and saturation artefacts appear depends on the photophysics of the fluorophore under given conditions and on the average time it undergoes excitation (which depends on detection volume dimensions and D) [150]. For typical organic fluorophores, excitation intensities should be sufficiently lower than 30 kW cm^{-2}, a value which corresponds for usual microscope objectives to excitation powers of approximately 100 μW [102, 148]. Excitation powers of less then 10 μW at back objective aperture were used in FCS experiments described in this thesis.

Detector afterpulsing (dark counts generated by the detector after a photon

detection event) is another source of artefacts in FCS. It distorts the autocorrelation curve in the region of short lag times τ, which distortion can be easily misinterpreted as a result of a large fraction T of fluorophores undergoing conversion to triplet state [151, 152]. A combination of FCS with time correlated single photon counting (TCSPC) called fluorescence lifetime correlation spectroscopy (FLCS) is able to eliminate the influence of detector afterpulsing on $G(\tau)$ [151, 152]. A pulsed laser is used in this method as the excitation light source and the arrival time of each detected photon is recorded on two different time-scales: a picoseconds scale measures its arrival time relative to the excitation pulse and a nanoseconds scale measures its arrival time relative to the beginning of the experiment. The contribution of each photon to the autocorrelation function $G(\tau)$, which is calculated using the arrival times on the nanosecond scale, is weighted by a statistical filter function according to its arrival on the picosecond scale. In that manner, only photons originating from a fluorophore characterized by a certain pattern of fluorescence decay after the excitation pulse can be selected to effectively contribute to $G(\tau)$ [152-154]. Detector afterpulsing is characterized by a uniform distribution of arrival times, while fluorescence exhibits an exponential decay after the excitation pulse. Therefore, the distortion of the autocorrelation curve caused by afterpulsing is efficiently avoided by FLCS. Photons of scattered light (distinguished by very short arrival times after excitation pulse) can be eliminated in an analogous way [152]. FCS experiments described in this thesis were performed either on MicroTime 200 (PicoQuant, Berlin, Germany) [153] or on Confocor 1 (Carl Zeiss, Jena, Germany; Evotec Biosystems, Hamburg, Germany) [155] confocal microscope. Both instruments are equipped with TCSPC units and pulsed diode lasers as excitation light sources; FLCS filtering (using software developed by Aleš Benda [156]) was always performed during $G(\tau)$ calculation to eliminate influence of detector afterpulsing.

4.5. Molecular diffusion in SLBs investigated by FCS

The theoretical models of $G(\tau)$ (4.7, 4.10, 4.11) were derived for fluorescent particles diffusing freely in 3-dimensions. However, when mobility of molecules in SLBs (or any other planar system such as molecular monolayers on air-water interfaces) is investigated by FCS, models describing diffusion confined to a 2-

dimensional plane must be used. Those are considerably simpler, because integration in (4.5) is done in *XY*-plane only [104]. Equation (4.12) is, then, the 2-dimensional counterpart of model (4.10) [127, 134, 157].

$$G(\tau) = 1 + \left[1 - T + T \exp\left(-\frac{\tau}{\tau_T} \right) \right] \frac{1}{N(1-T)} \frac{1}{1 + (\tau / \tau_D)} \tag{4.12}$$

All results of FCS in SLBs presented in this thesis were obtained by fitting measured $G(\tau)$ with model (4.12).

Positioning of the planar sample to the focal plane is a critical step in 2-dimensional FCS and an important source of experimental errors [158]. Assuming a Gaussian-Lorentzian profile $W_{GL}(R,Z)$ of the detection volume (4.1), the dependence of the illuminated area (the effective detection area) radius ω on the axial position of the planar sample is given by (4.2) (when the focal plane corresponds to $Z = 0$). Taking into account the dependence of τ_D and N on the size of the effective detection area (4.13a,b), where C_S is the surface concentration of fluorescent particles (number of fluorescent particles per unit area), it is obvious how the results of FCS depend on axial positioning of the planar sample (see figure 4.3 A) [127, 158].

$$\tau_D(\omega) = \frac{\omega^2(Z)}{4D} \tag{4.13a}$$

$$N(Z) = C_S \, \pi \, \omega^2(Z) \tag{4.13b}$$

The dependence on axial positioning hampers comparability between results of individual measurements and absolute determination of D and C_S, because the actual diameter ω of the detection area may not be equal to the focus waist ω_0 determined in calibration measurement (not mentioning the difference of focus waist ω_0 in the reference solution used for calibration and in the sample caused by a difference of refractive indices of the respective media, which is, however a general problem present also in 3-dimensional FCS).

Those problems motivated development of a variety of calibration-free FCS techniques, which do not need any external calibration because a certain distance measure is intrinsically present in each measurement. The techniques are reviewed for example in *Attachment I*. FCS measurements on SLBs presented here were done by *Z*-scan FCS, a calibration-free method pioneered by Aleš Benda et al. [127].

The principle of *Z*-scan FCS is illustrated in figure 4.3. It is based on measuring fluorescence autocorrelation functions $G(\tau)$ with the sample at different axial positions with a step-size typically of 100 or 200 nm. Substitution of (4.2) to (4.13a,b) yields the theoretical dependence (4.14a,b) of diffusion time τ_D and particle number N on axial position Z [104, 109, 127].

$$\tau_D(Z) = \frac{\omega_0^{\,2}}{4D}\left(1+\frac{\lambda^2 Z^2}{\pi^2 \omega_0^{\,4}}\right) \tag{4.14a}$$

$$N(Z) = C_S\, \pi\, \omega_0^{\,2}\left(1+\frac{\lambda^2 Z^2}{\pi^2 \omega_0^{\,4}}\right) \tag{4.14b}$$

Parabolic fits of the measured dependences $\tau_D(Z)$ and $N(Z)$ with model (4.14a,b) yield the physically relevant parameters D, C_S and ω_0 together with the exact axial position of the focal plane. The experimentally obtained parabolic dependences are often not exactly symmetric (see figure 4.3 C), which results probably from asymmetry of the detection volume when it is located at the interface between two media (solid support and aqueous solution). Misalignment of the axial position of the confocal pinhole represents an additional source of detection volume asymmetry, which is frequently encountered when more excitation wavelengths are used simultaneously in the microscope; the optimal axial pinhole position is wavelength dependent and a compromise between optima for individual wavelength has to be sought. The maximum of fluorescence intensity (photon count-rate) often does not coincide exactly with the minima of $\tau_D(Z)$ and $N(Z)$ [127]. It is usually caused by the detection volume asymmetry and shows that the maximum of photon count-rate is not a reliable indicator of positioning the sample to the focal plane.

Lateral diffusion of lipids in SLBs is a topic frequently addressed by FCS. The investigated SLB must contain a fluorescently labelled lipid or lipid analogue, diffusion of which is followed by FCS. Ratios of fluorescent lipids to native lipids are usually chosen in the range of $1{:}10^5$ to $0.5{:}10^5$ to reach the average number of fluorescent lipids per detection area close to 1 (giving the highest signal-to-noise ratio) [127]. Relevance of the measured diffusion coefficient of the fluorescently labelled lipid to the diffusion coefficient of native lipids is discussed in section 5.4 of *Attachment I*.

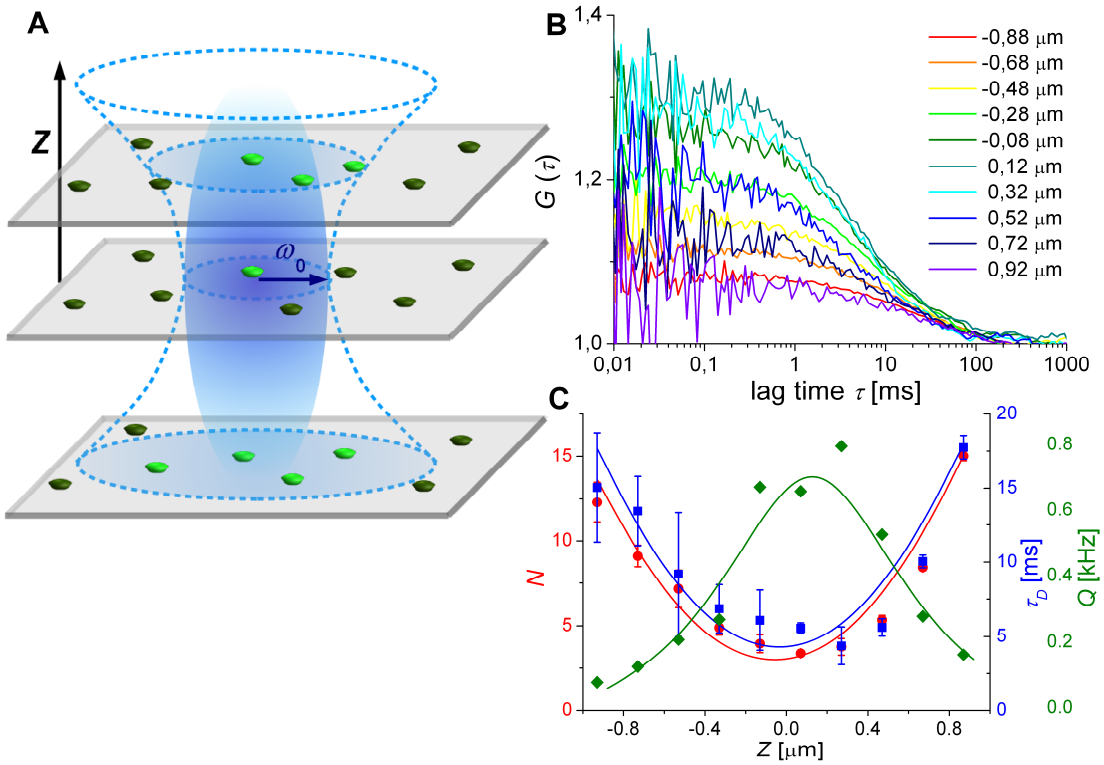

Figure 4.3: *Z*-scan FCS and the positioning problem of planar samples. Due to the divergence of the beam, positioning of a planar sample out of the focal plane results in a larger detection area and, thus, higher τ_D and N (**A**). In *Z*-scan FCS, measurements are performed with sample at different axial positions Z (focal plane corresponds to $Z = 0$) (**B**) and the dependences of τ_D and N on Z are analyzed (**C**). Data from a measurement of lipid diffusion in an SLB are shown. The Z dependence of photon count-rate per particle Q reflects the axial intensity profile of the beam, which is assumed to have a Lorentzian shape.

4.6. FCS diffusion laws

Deviations from free Brownian diffusion are sometimes encountered in biological membranes and SLBs containing lateral inhomogeneities [159-162]. Analysis of such deviations and their confrontations with theoretical models can provide important information on lateral organization of the membranes and their inhomogeneities. If the deviations are large enough, model (4.12), and other analogous models derived for freely diffusing molecules, fails to fit experimental autocorrelation functions satisfactorily and models for anomalous diffusion need to be used (*Attachment I*). However, even in cases when the inhomogeneities are

manifested in much subtler manner, useful information on membrane inhomogeneities and the way how they hinder molecular diffusion can be obtained from diffusion laws analysis.

The method analyses dependence of diffusion characteristics on the size of the area within which diffusion is investigated. The dependence is determined by the ratio of characteristic dimensions of the probed area to characteristic dimensions of the inhomogeneities. Three regions can be distinguished: *i)* locally, the molecules diffuse freely (normal diffusion); *ii)* their diffusion is anomalous for intermediate areas and *iii)* it can become normal again (but with a lower diffusion coefficient than in the absence of obstacles) when diffusion over areas much larger than size of the inhomogeneities is probed. Diffusion laws are particularly useful in the third region, where any single experiment would yield normal diffusion, nevertheless, the diffusion laws analysis can identify inhomogeneities in the SLB and provide information on their influence on molecular diffusion. The transition to normal diffusion shifts to larger probed areas with increasing fraction of total sample area occupied by the obstacles [163, 164].

In FCS, diffusion laws analysis requires measurement of FCS autocorrelation curves for different detection area diameters ω [165, 166]. In the case of free diffusion, diffusion time τ_D is directly proportional to detection area size (4.13a); deviations from proportionality between τ_D and ω^2 indicate hindrance of diffusion by inhomogeneities in the membrane. In the case of large detection areas (where the diffusion is apparently normal), a linear dependence (4.15) of τ_D on ω^2 is observed.

$$\tau_D = t_0 + \frac{\omega^2}{4D_{eff}} \qquad (4.15)$$

The intercept t_0 equals 0 in the case of a free Brownian diffusion, but it can take non-zero values when the diffusion is hindered. The effective diffusion coefficient D_{eff} is, then, different from the apparent diffusion coefficients measured at single values of ω. The value of t_0 can distinguish between two types of lateral inhomogeneities which are likely to be encountered in biological membranes. A positive value of t_0 indicates isolated microdomains, into which the fluorescent tracer molecule can partition with a certain probability and in which it undergoes a slower diffusion. Negative t_0, on the other hand, indicates membrane divided into corrals (for example

by actin meshwork); fluorescent tracer diffuses freely within a corral but it needs certain amount of energy to cross the barrier to an adjacent corral. Impermeable obstacles do not result in nonzero values of t_0; only reduce the diffusion coefficient [165, 167]. More information on diffusion laws can be found in section 2 of *Attachment I* and references cited therein.

Since each *Z*-scan measurement consists inherently of FCS recordings with different values of $\omega(Z)$, *Z*-scan represent the most straightforward experimental implementation of FCS diffusion laws [168]. Substitution of (4.2) to (4.15) and (4.13b) yields a dependence of τ_D on normalized particle number (4.16), where $N_0 = C_S \pi \omega^2$ is the particle number measured when the SLB is in the focal plane.

$$\tau_D = t_0 + \frac{\omega_0^2}{4D_{eff}} \frac{N}{N_0} \tag{4.16}$$

An example of plots of $\tau_D (N/N_0)$ (sometimes called Humpolíčková plots) can be found in figure 2 in *Attachment IV*. Free diffusion of a fluorescently labelled lipid in an SLB ($t_0 = 0$) is compared with hindered diffusion ($t_0 > 0$) of the same labelled lipid in the presence of microdomain-like obstacles induced in the SLB by peptide arenicin-1. It is important to note that by diffusion laws analysis, information can be obtained on inhomogeneities significantly smaller than resolution of optical microscopy [167, 169].

5. Antimicrobial peptides and their interactions with lipid membranes

5.1. Antimicrobial peptides and their biological activity

Antimicrobial peptides are a very large and varied collection of peptides found in all multicellular organisms. They play a key role in the innate immunity, which, in spite of being evolutionary very old, has lost nothing of its efficiency in enabling multicellular organisms to survive amidst millions of microbes [6, 170]. Main features of AMPs have been preserved during the evolution, showing that they have withstood the test of time as an efficient protection against pathogens. AMPs are typically active against a broad range of microorganisms (Gram-positive or Gram-negative bacteria, fungi and even enveloped viruses [6, 171]), though some of them exhibit specificity only against certain classes of microbes, and most AMPs have low toxicity for eukaryotic cells [6, 170, 172]. Furthermore, very few bacterial species show resistance to AMPs and development of resistant mutants does not seem a simple process [6, 170, 173]. The above mentioned characteristics make AMPs (or their synthetic analogues) a very perspective alternative to traditional antibiotics, against which an increasing number of pathogens have developed resistance [174]. Additionally AMPs have been studied as potential antitumor or antiseptic agents or food preservatives [175-178].

All that explains the unceasing attention AMPs have been receiving over the past decades. Peptides from a large variety of organisms have been isolated and characterised [6] and modified natural peptides or artificially designed peptides have been synthesized in order to optimize efficiency and selectivity of AMPs [2, 3] or to investigate dependence of AMPs' activity on their charge, hydrophobicity and other characteristics [179-181]. Nevertheless, in spite of concentrated research, the exact mechanism of AMPs biological activity has not been explained in full detail. Among findings firmly established by extensive experimental evidence is the fact that AMPs do not kill cells via interaction with protein receptors. The conclusion is based on lack of chiral specificity in AMPs activity (all-D enantiomers are equally active) [182, 183] and is further supported by large variety of amino acid sequences among AMPs [6, 184].

In spite of the large variability in primary sequences, AMPs share some

common characteristic in the physicochemical properties of their molecules, namely the net positive charge and amphiphilic character, which are certainly essential for their activity [170, 184, 185]. AMPs are known to permeate lipid bilayers; it is, therefore, believed that they kill target cells via membrane permeation, which leads to dissipation of vital transmembrane gradients [5, 186]. Several models of membrane permeation by AMPs have been proposed [7, 186, 187]; the so called toroidal pore seems the most likely model for many AMPs [7, 188-190]; though evidence for other mechanisms of action (such as barrel-stave pores or detergent-like effects) has been also reported for some peptides [186, 191, 192].

The direct peptide-membrane interactions can also explain the selectivity of most AMPs against prokaryotic cells. While outer leaflet of eukaryotic membranes is composed almost entirely of electronegative lipids (mostly phosphatidylcholine and sphingomyelin), outer leaflets of bacterial membranes contain also negatively charged lipids (mainly phospatidylglycerol and cardiolipin) and outer membranes of Gram-negative bacteria are covered with polyanionic lipopolysaccharides, while Gram-positive bacteria contain anionic teichoic acid in their peptidoglycan wall [7, 172]. Since AMPs are cationic, they preferentially associate with negatively charged lipid membranes. Cytolytic peptides from venoms (such as melittin) contain, on the other hand, more hydrophobic domains which facilitate their insertion to electronegative (eukaryotic) membranes via hydrophobic interaction [172, 193, 194]. The explanation of AMPs' selectivity based on electrostatic interactions is further supported by findings that bacterial strains exhibiting resistance to several AMPs have lower density of anionic lipids in their membranes or reduce their negative surface charge by esterification of teichoic acid with D-alanine [6, 195]. Presence of sterols in membranes of eukaryotic cells represents another difference between eukaryotes and prokaryotes, which may play a role in AMPs' selectivity; it has been indeed reported that efficiency of lipid bilayer permeation by various AMPs is decreased by presence of cholesterol in the lipid bilayer [7, 187, 196].

Cytoplasmic membrane is, however, not the only possible target of AMPs and evidence for intracellular targets has been reported [170, 197, 198]. It is possible that formation of pores in cytoplasmic membrane is only one of several steps in the mechanism by which AMPs kill their target cells. Although the membrane permeation may be lethal by itself, it also allows peptide molecules to enter into the

cell, where they can attack further targets; nucleic acids as polyanionic molecules represent a likely target for cationic AMPs [170, 197]. Nevertheless, those findings do not deny the importance of biological membranes as target structures for AMPs; if the plasma membrane is not the only target of the peptide in the cell, it is at least the first structure with which the peptide must interact on its way to intracellular targets. Therefore, investigation of interaction of AMPs with biological membranes and their artificial models remains essential for understanding the biological activity of the peptides.

The peptides investigated in studies presented here are summarized below with their basic characteristics and references to Attachments and selected publications:

Cryptdin-4 (GLLCYCRKGHCKRGERVRGTCGIRFLYCCPRR, + 8.5 charge at physiological pH) is the most bactericidal of the α-defensins produced by mouse Paneth cells [199-202] and has a relatively rigid secondary structure of three β-strands stabilized by three disulphide bonds, which is typical of defensins [6, 201] (see *Attachment II*).

Magainin 2 (GIGKFLHSAKKFGKAFVGEIMNS, + 4 charge at physiological pH), isolated from skin of African frog *Xenopus laevis* is killing bacteria with high efficiency and selectivity [172, 183, 203, 204]. Its secondary structure is widespread among AMPs; the peptide is linear in aqueous solutions and adopts an amphiphilic α-helical conformation in membranes or membrane-mimetic environments [6, 187, 191] (see *Attachment II*).

Melittin (GIGAVLKVLTTGLPALISWIKRKRQQ, + 6 charge at physiological pH) is the main component of bee (*Apis mellifera*) venom. It is strictly speaking not an antimicrobial peptide, because it has low selectivity against microbes (has high haemolytic activity), but is traditionally included among AMPs [188, 193, 194]. It is another example of linear peptides adopting α-helical conformation in membranes [205-207] (see *Attachment III*).

Arenicin-1 (RWCVYAYVRVRGVLVRYRRCW, + 6 charge at physiological pH) was isolated from marine polychaeta *Arenicola marina* [208]. It forms an 18-residue ring stabilized by a disulphide bond and possesses broad-spectrum activity against

Gram-positive and Gram-negative bacteria and fungi [92, 209] (see *Attachment IV*).

LAH_4 (KKALLALALHHLAHLALHLALALKK) is a model linear peptide adopting α-helical conformation in membranes. Although it was designed primarily as a model sequence to study peptide helix orientation in lipid bilayers, it proved to be also en efficient antimicrobial peptide [210]. The four histidine residues allow pH-dependent manipulation of the peptide net positive charge, which changes from + 9 at acidic pH (lower than approximately 6) to + 5 at higher pH [187, 210]. The different values of electrostatic charge have been found to correspond to different orientations of the peptide helices in membranes, which is transmembrane at higher and parallel to membrane surface at lower pH [181, 211, 212]; the pH-dependent changes in peptide charge an orientation also influence its antimicrobial activity [210, 213] (see *Attachment V*).

Influence of the peptides on artificial lipid membranes was investigated by characterizing AMP-induced changes in morphology (thickness and lateral distribution of lipids) and fluidity (lateral diffusion of lipids) of SLBs. The studies are briefly explained in sections 5.2 to 5.4 and more details can be found in the respective Attachments. Since AMPs are known to permeate biological membranes, studies of peptide-induced release of molecules from liposomes are important for understanding membrane-peptide interactions. FCS can be very useful in such studies [214, 215]. The method is, however, not described here, because it is beyond the scope of this thesis dealing with SLBs and their interactions with AMPs. More details on the method can be found in *Attachment V*.

5.2. SLB morphology - lipid tubules and other lateral inhomogeneities

Peptide-induced morphological changes in SLBs were characterized mainly by combination of ellipsometry and LSM. Ellipsometry measures thickness of the adsorbed layer on nanometre scale and provides information on the layer mass (which is related to the density of molecules in the layer); it, however, lacks lateral resolution, because the data are collected from a relatively large area of the surface (approximately 6 mm^2) defined by the reflected laser beam. LSM supplemented the missing information on lateral inhomogeneities in the bilayer (with resolution limited by resolving power of confocal microscopy). Furthermore, changes in fluorescence

intensity in LSM scans can be quantitatively interpreted in terms of changes in lipid density in the bilayer (provided that the fluorescently labelled lipids are distributed homogeneously among lipids in the sample). That allows separation of contributions of lipids and of the peptide to the mass of the adsorbed layer which is measured by ellipsometry. In order to draw conclusions on peptide-induced changes in lipid density from changes in fluorescence intensity, all other mechanisms by which presence of the peptide may influence fluorescence intensity (for example fluorescence quenching) have to be taken into account.

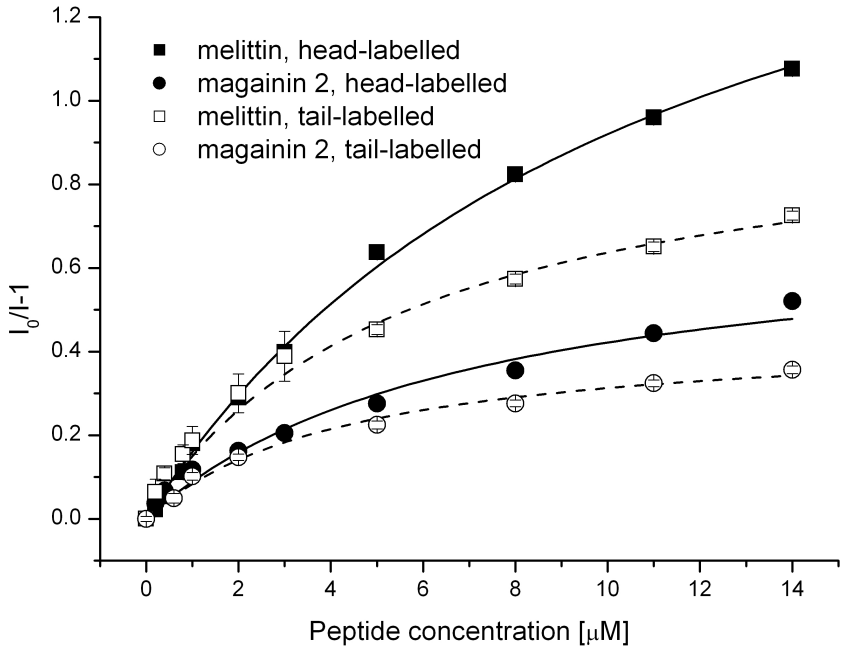

Figure 5.1: Peptide-induced decrease of fluorescence intensity (*I* is the actual intensity and I_0 the intensity prior to peptide addition) of a suspension of SUVs; a bulk measurement using Fluorolog-3 (Horiba Jobin Yvon, France). SUVs were composed of DOPC and DOPS in molar ratio 4:1 and fluorescently labelled lipid was added in ratio 1:1000 native lipids. Lipids with fluorophore bound to the headgroup (BODIPY FL-1,2-dihexadecanoyl-*sn*-glycero-3-phosphoethanolamine) or hydrophobic tail (2-(β-BODIPY 500/510)-1-hexadecanoyl-sn-glycero-3-phosphocholine), both purchased from Invitrogen (Carlsbad, CA), are compared; note that head-labelled lipid is quenched more efficiently.

A simple control experiment was performed to assess the influence of investigated peptides on fluorescently labelled lipids used in our studies. Suspensions

of SUVs of desired lipid composition containing fluorescently labelled lipids (in the same ratio of labelled to native lipids as in the investigated SLBs) were titrated by solutions of the studied AMPs and bulk fluorescence of the suspensions was monitored by a steady-state fluorescence spectrometer. Since changes in lipid density in the membranes of SUVs do not influence the number of fluorescently labelled lipids present in the probed sample, observed decrease in fluorescence intensity was attributed to quenching of the fluorescently labelled lipids by the peptide. Figure 5.1 shows an example of such experiment for peptides magainin 2 and melittin. Results of the control experiments were, then, used in interpretation of intensities of LSM scans.

An example of exploitation of all information on changes in SLB morphology provided by parallel LSM and ellipsometric experiments can be found in *Attachment III*. SLBs on glass were treated with melittin in concentrations from 0.1 to 3 μM and the evolution of thickness d and mass Γ of the layer was monitored in time after peptide addition to the sample; the experiments were terminated by washing away melittin from the sample by excess of peptide-free buffer and measuring resulting mass and thickness. It was found that the melittin-induced changes in d and Γ reach their full magnitude at 0.5 μM peptide concentration and higher concentrations (up to 3 μM) do not cause any larger effects. Addition of melittin causes rapid decrease in layer mass Γ (approximately 25 %), which is accompanied by a slightly slower growth of thickness d (see figure 3 in *Attachment III*). While the decrease in mass can be explained by decreased lipid density in the layer due to formation of pores or other membrane defects (the superfluous lipids being probably removed to the aqueous phase in the form of lipid-peptide micelles), which is the generally accepted mode of action of melittin, the explanation of the growing thickness required additional information provided by LSM.

LSM (see figure 1 in *Attachment III*) revealed formation of many lateral inhomogeneities in the SLBs treated with 1 μM melittin. We assume that the long thin structures (with thickness below resolution of confocal microscopy) are lipid tubules characterized previously by Domanov and Kinnunen [216]. They investigated interaction of several α-helical AMPs with SLBs and observed formation of long protruding structures, which they found to be lipid bilayer tubules. One end of the tubule is attached to the bilayer and the rest of the tubule is moving

freely in the aqueous phase above the SLB. It can be noted in figure 1 in *Attachment III* that all tubules are oriented in one direction. That is caused by continuous stirring of the sample; the resulting flow of the aqueous phase above the SLB aligns all tubules in one direction parallel to the surface of the bilayer. The tubules assumed random orientations when stirring was stopped after they had been formed (see figure 5.2 A). The hydrodynamic force of the flow is essential for formation and stability of the tubules; we observed no formation of tubules in the absence of stirring (see figure 5.2 B-D), which agrees with Domanov's observations that tubules can be stretched longer by increasing applied hydrodynamic force, while too high forces can detach the tubules from the SLB surface (Y. Domanov, personal communication). Like Domanov and Kinnunen [216], we occasionally observed collapse of a tubule into a smaller multilamellar structure resembling the inhomogeneities induced by melittin in the absence of stirring (figure 5.2 C). Such structures are more rigid and, therefore, protruding more from the SLB surface into the aqueous phase above. They are, most likely, responsible for the large increase in thickness of the adsorbed layer measured by ellipsometry, which occurred between 1500 and 5000 s after peptide addition (figure 3 C, D in *Attachment III*). The absence of the large increase in thickness when faster stirring (and, thus, higher hydrodynamic force) was applied proves the importance of hydrodynamic force for tubule stability.

Apart from the tubules, structures of higher fluorescence intensity occupying larger area appear in the LSM scans (see for example the upper row of scans in figure 1 in *Attachment III*). Their fluorescence intensity (determined from *XZ*-scans) is approximately three times higher than in the surrounding bilayer and we, therefore, assume them to be bilayer stacks consisting of three bilayers. Occasionally, stacks consisting of 5 bilayers were also observed. Analogous stacks were also observed by Domanov and Kinnunen (Y. Domanov, personal communication), who proposed a model of their structure shown in figure 5.3. The lipid density (inferred from fluorescence intensity in *XZ*-scans) of the bilayer (outside of the inhomogeneities) decreased to approximately 60 % of its initial value. That finding is consistent with formation of pores in the bilayer; part of the superfluous lipids forms the above described stacks and tubules, while the rest probably desorbs in the form of lipid-peptide micelles. Almost all lateral inhomogeneities in the membrane were removed

when the sample was flushed with melittin-free buffer.

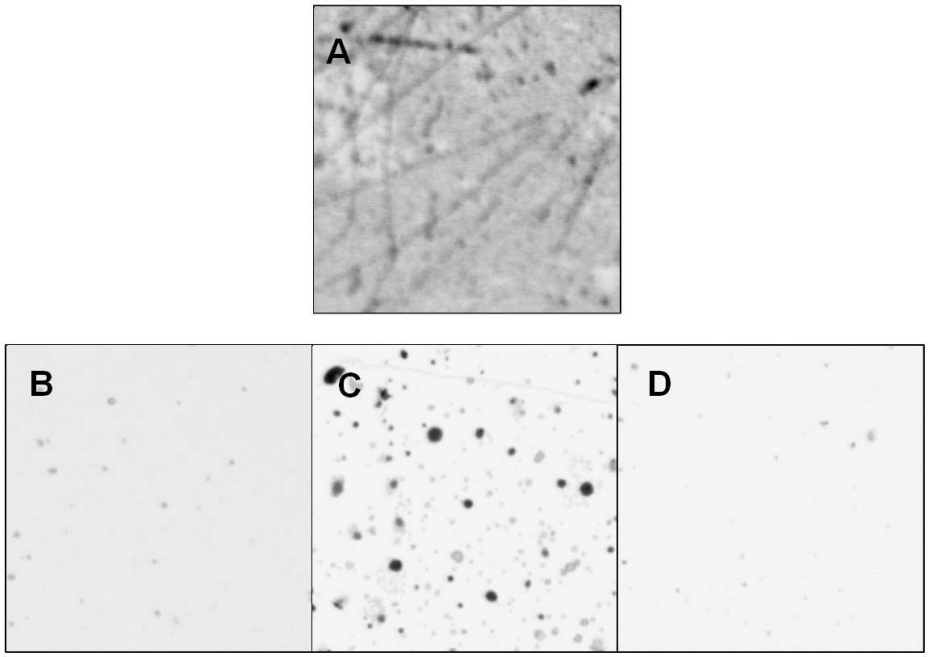

Fig 5.2: LSM scans of SLBs on glass support in buffer: 10 mM HEPES, 150 mM NaCl, 2 mM ethylenediaminetetraacetic acid (EDTA), pH 6.9. The SLB was composed of DOPC and DOPS in molar ratio 4:1 and contained fluorescently labelled lipid (2-(β-BODIPY 500/510)-1-hexadecanoyl-sn-glycero-3-phosphocholine) in ratio 1:1000 native lipids. Panel **A** shows SLB approximately 15 minutes after it has been exposed to 1 μM melittin; the sample was stirred for approximately 10 minutes after peptide addition and than stirring was stopped. Remaining panels show scans of an SLB treated with 1 μM melittin in the absence of stirring; the initial bilayer (**B**), the SLB 90 minutes after peptide addition (**C**) and after flushing with excess of melittin-free buffer (**D**) are shown. Darker shades correspond to higher fluorescence intensity; the size of the scans is 30 × 30 μm except of panel **A**, in which it is 20 × 20 μm.

To learn more about the melittin-induced changes in membrane morphology on length-scales below resolution of confocal microscopy, SLBs prior to and after treatment with 1 μM melittin were also imaged by AFM. Representative images displayed in figure 5.4 show increased roughness of the SLB (in agreement with [217]) after addition of melittin but do not provide any information concerning pores or tubules. AFM imaging of melittin-induced pores is very difficult because of

combined effect of their small dimensions (values in the range 1 – 6 nm have been reported in the literature [190, 218]) and large local gradients in height [219]. Therefore, their absence in the AFM image does not exclude their presence in the bilayer. It is not surprising that tubules were not observed by AFM, considering the importance of stirring (which is not possible during AFM imaging) for their formation and stability. Furthermore, they would be very likely detached from the SLB surface by the AFM tip moving in their vicinity.

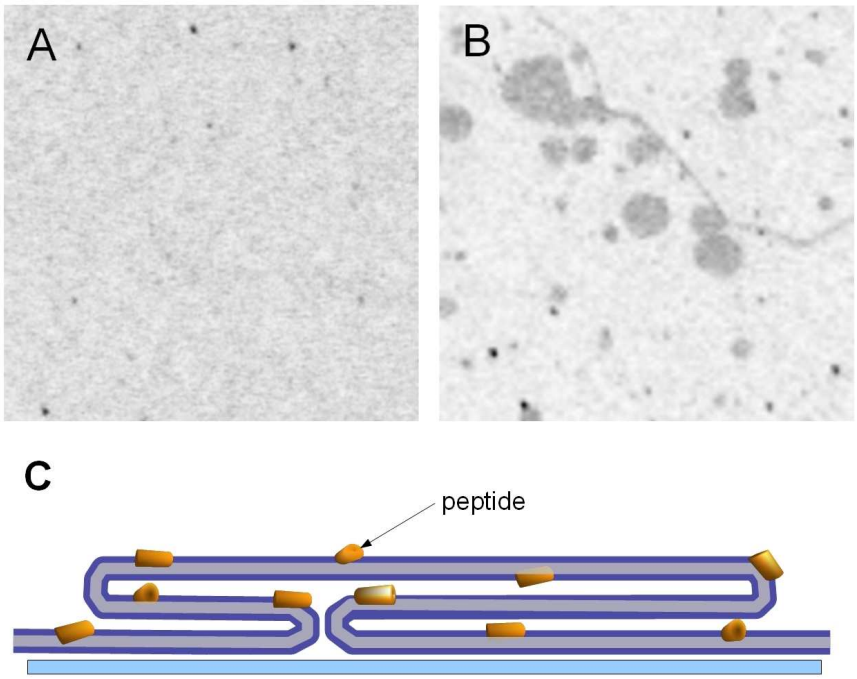

Fig 5.3: LSM scans of 1-palmitoyl-2-oleoyl-phosphatdylcholine (POPC) SLBs on glass support at pH 8. The SLB is visible thanks to presence of fluorescently labelled lipid (for details see figure 5.2 caption). The initial state of the bilayer (**A**) and the bilayer after addition of LAH_4 (0.2 µM total peptide concentration in the sample) (**B**) are shown. Darker shades correspond to higher fluorescence intensity; the size of the scans is 30 × 30 µm. Areas of higher intensity can be noted in panel **B**; their average fluorescence intensity is approximately 3 times higher than intensity of the surrounding bilayer (47 ± 5 vs. 15 ± 3 arbitrary units), which suggests they are stacks consisting of 3 bilayers. A hypothetic model of such stack is shown in panel **C**.

Melittin-induced tubules were also imaged with higher resolution by DSOM (data not shown). Combination of long image acquisition times needed in DSOM and

of movement of the flexible tubules (attached to the SLB only in one point) yielded their imaging with higher resolution impossible. Furthermore, the fluorescently labelled lipids in the tubule walls were not moving fast enough to avoid photobleaching during the long image acquisition.

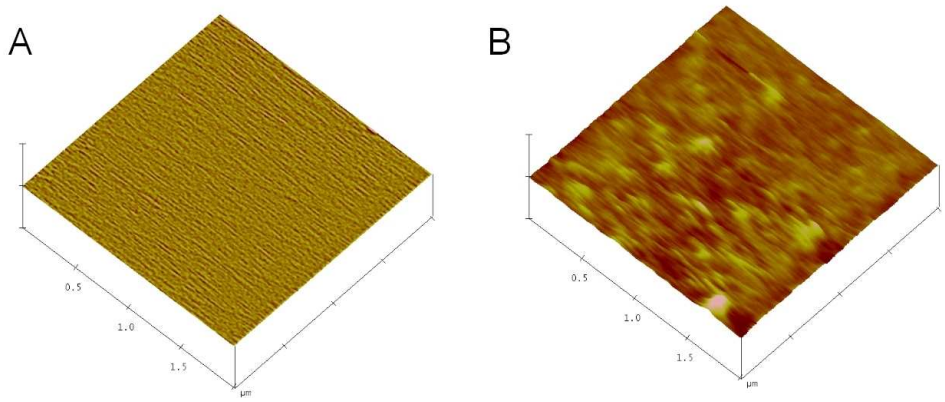

Fig 5.4: AFM images of SLB composed of DOPC and dioleoyl-phosphatidylglycerol (DOPG) (7:3 molar ratio) on mica before (**A**) and after (**B**) addition of 1 µM melittin. Imaging was performed in buffer: 10 mM HEPES, 150 mM NaCl, 2 mM EDTA, pH 6.9. The scans were recorded by Nanoscope III (Digital Instruments, Santa Barbara, CA) in tapping mode. Size of the scans is 2 × 2 µm and the vertical (*Z*) scale is 10 nm. Root-mean-square roughness R_q of the SLB calculated according to (3.1) increased from 0.09 nm (**A**) to 0.20 nm (**B**).

Analogous experiments were done also for other peptides. In the case of magainin 2 a significant decrease in bilayer mass was also accompanied by an increase in thickness, which can be explained by formation of small membrane protrusions (*Attachment II*). Formation of bilayer stacks consisting of three lipid bilayers was also observed in the case of SLBs treated with 0.2 µM LAH_4 at basic pH (when the peptide bears higher positive charge; representative LSM scans are shown in figure 5.3), while at acidic pH, the peptide induced no change in SLB morphology. Neither were any significant changes in lipid distribution observed in the cases of SLBs treated with cryptdin-4 (*Attachment II*) or arenicin-1 (*Attachment IV*). In conclusion it can be said that AMPs adopting α-helical conformation in membrane-like environments disturb the structure of lipid bilayers to much larger extent than peptides with rigid structures stabilized by disulphide bonds; however, more AMPs would have to be compared to draw conclusions on relationship between

secondary structure and mode of action

5.3. AMPs and membrane lipid diffusion

Lipid diffusion in SLBs was measured by *Z*-scan FCS in order to estimate the influence of the peptides on lipid bilayer fluidity. Changes in membrane fluidity, an important property of biological membranes, may be a part of the biological effects of AMPs. Furthermore, analysis of lipid diffusion in terms of FCS diffusion laws can reveal information on lipid organization in the bilayer and its inhomogeneities on length scales below the resolution of optical microscopy (see section 4.6).

Attachment IV shows how information on lipid diffusion obtained by *Z*-scan FCS can elucidate mode of action of an AMP. SLBs were titrated with arenicin-1 up to 3 μM concentration and *Z*-scan measurements were performed after each peptide addition. While in purely zwitterionic (DOPC) SLBs, lipid diffusion was not influenced by increasing arenicin-1 concentration, diffusion of lipids in negatively charged SLBs (DOPC:DOPS 4:1) was significantly slowed by arenicin-1 in concentrations larger than 1 μM (see figure 1 in *Attachment IV*). Speed of lipid diffusion can be reduced by increased order and rigidity of the bilayer caused by incorporation of peptide molecules and/or by formation of obstacles (such as pores and lipid-peptide aggregates) which hinder the diffusion. Diffusion laws analysis was, therefore, performed to obtain insight into the mechanism by which arenicin-1 influences lipid diffusion.

The analysis revealed that slowing of lipid diffusion in anionic SLBs is accompanied by formation of inhomogeneities, which have the character of microdomains. The conclusion is based on the values of intercept t_0 in Humpolíčková plots; its average value prior to peptide addition was $t_0 = (0.5 \pm 1.1)$ ms (in agreement with free lipid diffusion) and it reached a significantly higher value $t_0 = (10.2 \pm 5.1)$ ms at 2 μM arenicin-1 corresponding to the large decrease in lipid diffusion coefficient (see figure 2 in *Attachment IV* for representative Humpolíčková plots). No change in the intercept t_0 was observed in the case of purely zwitterionic SLBs, where its average value at 2.8 μM peptide concentration $t_0 = -(0.2 \pm 1.2)$ ms is consistent with free lipid diffusion.

Our explanation of peptide-induced microdomain formation in SLBs containing anionic lipids is based on the model of arenicin-2 (an isoform of arenicin-

1) association with lipid membranes proposed by Ovchinnikova et al. [220]. Based on the peptide secondary structure in membrane-mimetic systems, they assume that the peptide associates with membranes in the form of dimers, which, at higher peptide concentrations, associate to tetramers stabilized by anionic lipid headgroups; accumulation of peptide tetramers induces curvature strain in outer membrane leaflet, which eventually leads to transition of peptide tetramers to transmembrane orientation accompanied by opening of toroidal pores. We conclude that arenicin-1 dimers also form tetramers stabilized by anionic lipid headgroups and that those tetramers can associate further into larger structures which, besides peptide molecules and anionic lipids, also contain neutral lipid molecules with considerably hindered mobility. Lipid molecules (including the fluorescently labelled lipid) can enter and leave the peptide-lipid domains giving rise to positive values of the intercept t_0.

Similar trends were also observed in the case of melittin and its interaction with SLBs containing anionic lipids. Representative Humpolíčková plots obtained for a bilayer composed of POPC and 1-palmitoyl-2-oleoyl-phosphatidylglycerol (POPG) in molar ratio 7:3 are shown in figure 5.5. The lipids diffuse freely in the SLB prior to peptide addition and the intercept t_0 of the Humpolíčková plots is close to 0, the average value from repeated experiments being $t_0 = (0.9 \pm 1.4)$ ms. 1 μM melittin decreased lipid diffusion coefficient to approximately 60 % of its original value (*Attachment III*) and the slowing of diffusion is accompanied by increase in the intercept to the value $t_0 = (9.7 \pm 0.4)$ ms. The positive value of t_0 indicates microdomain-like obstacles to lipid diffusion. Those obstacles are not necessarily domains of higher lipid order; they can be actually pores which are assumed to be present in SLBs treated with melittin (*Attachment III*). Toroidal pores, which have been shown to be formed in the presence of melittin [190, 221], are surrounded by a bilayer edge characterized by high curvature of the lipid layer (see figure 1.1). The lateral movement of a lipid within the region of high curvature surrounding a pore is likely to be slower than in the rest of the bilayer. Therefore, toroidal pores can possibly obstacle lipid diffusion in a manner similar to lipid microdomains. Other types of obstacles such as lipid-peptide domains analogous to those formed by arenicin-1 may be also present in the SLB. After the sample has been flushed with melittin-free buffer, intercept slightly decreased to the value $t_0 = (6.1 \pm 1.0)$ ms while

lipid diffusion coefficient did not change. The decrease in t_0 is probably connected with removal of melittin and some of the obstacles by exchange of buffer. The fact that the (apparent) diffusion coefficient remained unaltered is caused by a decrease in effective diffusion coefficient D_{eff}, defined by equation (4.15), upon exchange of buffer. D_{eff} depends on local diffusion coefficient in the obstacles and in the surrounding bilayer as well as on probabilities with which lipid molecules enter and exit the obstacles [165]; it is therefore difficult to speculate on the exact mechanism underlying its change. It is probably connected with changes in lipid density and, thus, in free area available in the bilayer, which influences local lipid diffusion coefficients (see section 2 of *Attachment I* and references cited therein for discussion of the free are theory of lipid diffusion).

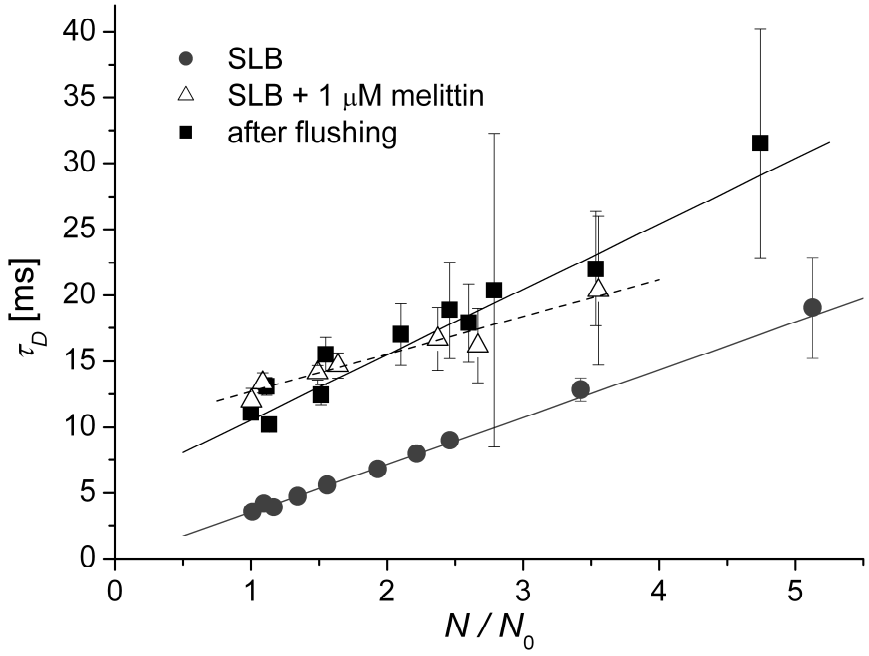

Fig 5.5: FCS diffusion laws analysis of influence of melittin on lipid diffusion in SLBs (POPC:POPG 7:3). Representative Humpolíčková plots of data measured in SLB before peptide addition (circles), after reaching 1 μM melittin concentration (triangles) and after flushing the sample with melittin-free buffer (squares) are shown. The error bars represent errors (estimated by the method of Wohland et al. [132]) in determination of diffusion time τ_D by fitting of FCS autocorrelation functions.

5.4. Peptide diffusion in SLBs

How are the peptide molecules distributed in the bilayer and how do they move along the bilayer plane? Those questions arose during interpretation of experiments described in previous sections (5.2 and 5.3), in which peptide-induced changes in lipid distribution and lipid mobility were investigated. Thanks to collaboration with Dr. Tatiana V. Ovchinnikova from Shemyakin and Ovchinnikov Institute of Bioorganic Chemistry (Moscow, Russia) who provided us with fluorescently labelled peptide, we were able to answer those questions for peptide arnicin-1 (*Attachment IV*).

LSM revealed no inhomogeneities (on the length scales accessible by confocal microscopy) in distribution of SLB-associated arenicin-1. More insight on arenicin-1 interaction with SLBs was provided by *Z*-scan FCS. Speed of peptide diffusion in both anionic and zwitterionic SLBs decreases with increasing peptide concentration. While the decrease in zwitterionic SLBs is gradual, a sharp drop in peptide diffusion coefficient was observed in SLBs containing anionic lipids (DOPC:DOPS 4:1) at 250 nM arenicin-1 concentration (see figure 3 in *Attachment IV*). Interestingly, the large change occurred at much lower arenicin-1 concentrations than the sharp drop in lipid diffusion coefficient. We conclude that the decrease in peptide mobility corresponds to formation of peptide oligomers and that a higher concentration of peptide oligomers is needed to significantly alter overall properties of the bilayer such as lipid diffusion coefficient (most likely via formation of peptide lipid microdomains). We can, therefore, speculate that the changes in lipid diffusion coefficient should be better correlated with biological activity of the peptide than diffusion of the peptide itself. That conclusion is supported by the correspondence of the ranges of arenicin-1 concentrations at which lipid mobility significantly decreases and at which bactericidal efficiency of the peptide increases [92, 209].

Diffusion laws analysis again revealed differences between SLBs containing anionic lipids and purely zwitterionic SLBs. While in the former system, the intercept t_0 reached positive values already at the lowest peptide concentration investigated (and slightly increased with increasing peptide concentration), no significant deviations of t_0 from zero were detected in zwitterionic (DOPC) SLBs.

Concluding remarks

The question of biological relevance of obtained results is an important concern in interpretation of all studies based on simplified artificial models of biological structures and, naturally, applies also to the use of SLBs as a model of biological membranes. It should be, therefore, discussed, at least briefly, in a work investigating membrane-activity of AMPs by studying their influence on SLBs.

The complexity of plasma membrane of any living cell is in marked contrast to the simplicity of typical artificial lipid bilayers, which can, therefore, never mimic all the factors influencing interaction of AMPs with membranes of living cells. That is, however, not a major concern. The aim of studies investigating interaction of AMPs with artificial lipid bilayers is not to predict the biological activity of those peptides (which is typically known from previous biological studies), but to contribute to elucidation of the molecular mechanism behind that activity. Simplified model systems are indispensable for that purpose, because they allow systematic investigation of individual factors that can influence peptide-membrane interaction such as surface charge or fluidity of the bilayer. It is therefore not surprising that most of experimental evidence on which, models of peptide-membrane interaction are based, was obtained using artificial lipid bilayers.

A more serious concern in interpretation of results obtained with artificial lipid bilayers is the influence of factors present in the model system, which are not present in biological membranes; a typical example is the vicinity of solid support in the case of SLBs. For example, formation lipid tubules induced by AMPs was observed for the first time in experiments on SLBs [216] and a doubt could arise whether the bilayer-support interactions are not involved in the process. Such doubts were however refuted by later studies reporting melittin-induced tubule formation also in the case free-standing bilayers (GUVs) [222]. It is, therefore, evident that, although the relevance of tubules to the *in vivo* effects of melittin may be to some extent questionable (the heterogeneous organization of plasma membranes of cells or absence of necessary hydrodynamic force may prevent formation of tubules *in vivo*), their formation is a result of melittin-bilayer interaction and provides evidence on influence of the peptide on physical properties of lipid bilayers and its knowledge is valuable for understanding mechanisms by which AMPs interact with biological

membranes. An important feature of all the experimental technique used within this work is their ability to investigate lipid bilayers in aqueous environment and, thus, under physiologically relevant conditions. Especially FCS has proved to be a very valuable tool in investigating the influence of antimicrobial peptides on lipid bilayers. It can probe changes in lipid organization in SLBs (*Attachments I-IV*) as well as permeation of liposomes (*Attachment V*), in which way it can provide a very comprehensive picture of mode of action of AMPs and other membrane-active compounds. Nevertheless, Interpretation of FCS results benefits considerably from information provided by other complementary methods such as ellipsometry.

References

[1] B. Findlay, G.G. Zhanel, F. Schweizer, Cationic amphiphiles, a new generation of antimicrobials inspired by the natural antimicrobial peptide scaffold, Antimicrob. Agents Chemother. 54 (2010) 4049-4058.

[2] E.B. Hadley, R.E.W. Hancock, Strategies for the discovery and advancement of novel cationic antimicrobial peptides, Curr. Top. Med. Chem. 10 (2010) 1872-1881.

[3] S.E. Blondelle, K. Lohner, Optimization and high-throughput screening of antimicrobial peptides, Curr. Pharm. Design 16 (2010) 3204-3211.

[4] L. Rivas, J.R. Luque-Ortega, M. Fernandez-Reyes, D. Andreu, Membrane-active peptides as anti-infectious agents, J. Appl. Biomed. 8 (2010) 159-167.

[5] Y. Shai, Mechanism of the binding, insertion and destabilization of phospholipid bilayer membranes by alpha-helical antimicrobial and cell non-selective membrane-lytic peptides, Biochim. Biophys. Acta-Biomembr. 1462 (1999) 55-70.

[6] M. Zasloff, Antimicrobial peptides of multicellular organisms, Nature 415 (2002) 389-395.

[7] A.A. Strömstedt, L. Ringstad, A. Schmidtchen, M. Malmsten, Interaction between amphiphilic peptides and phospholipid membranes, Curr. Opin. Colloid In. 15 (2010) 467-478.

[8] M. Luckey, Membrane structural biology with biochemical and biophysical foundations, Cambridge University Press, Cambridge, 2008.

[9] B. Alberts, A. Johnson, J. Lewis, M. Raff, K. Roberts, P. Walter, Molecular biology of the cell, 4th ed., Garland Science, New York, 2002.

[10] D. Marguet, P.F. Lenne, H. Rigneault, H.T. He, Dynamics in the plasma membrane: How to combine fluidity and order, Embo J. 25 (2006) 3446-3457.

[11] F.D. Gunstone, J.L. Harwood, A.J. Dijkstra (Eds.), The lipid handbook, CRC Press, Boca Raton, 2007.

[12] R. Hober, Membrane permeability to solutes in its relations to cellular physiology, Physiol. Rev. 16 (1935) 0052-0102.

[13] B.W. Vandermeer, R.D. Fugate, P.J. Sims, Complement proteins C5B-9 induce transbilayer migration of membrane phospholipids, Biophys. J. 56 (1989) 935-946.

[14] K. John, S. Schreiber, J. Kubelt, A. Herrmann, P. Müller, Transbilayer movement of phospholipids at the main phase transition of lipid membranes: Implications for rapid flip-flop in biological membranes, Biophys. J. 83 (2002) 3315-3323.

[15] M.A. Kol, A. de Kroon, D.T.S. Rijkers, J.A. Killian, B. de Kruijff, Membrane-spanning peptides induce phospholipid flop: A model for phospholipid translocation across the inner membrane of E-coli, Biochemistry 40 (2001) 10500-10506.

[16] J.N. Bai, R.E. Pagano, Measurement of spontaneous transfer and transbilayer

movement of bodipy-labeled lipids in lipid vesicles, Biochemistry 36 (1997) 8840-8848.

[17] R.D. Kornberg, McConnel.H.M., Inside-outside transitions of phospholipids in vesicle membranes, Biochemistry 10 (1971) 1111-1120.

[18] A. Kulakowska, P. Jurkiewicz, J. Sýkora, A. Benda, Y. Mely, M. Hof, Fluorescence lifetime tuning-a novel approach to study flip-flop kinetics in supported phospholipid bilayers, J. Fluoresc. 20 (2010) 563-569.

[19] S.J. Singer, G.L. Nicolson, Fluid mosaic model of structure of cell-membranes, Science 175 (1972) 720-721.

[20] R.S. Cantor, The lateral pressure profile in membranes: A physical mechanism of general anesthesia, Biochemistry 36 (1997) 2339-2344.

[21] M.A. Bahri, A. Seret, P. Hans, J. Piette, G. Deby-Dupont, M. Hoebeke, Does propofol alter membrane fluidity at clinically relevant concentrations? An ESR spin label study, Biophys. Chem. 129 (2007) 82-91.

[22] D.R. de Araujo, E. de Paula, L.F. Fraceto, Local anesthetics: Interaction with biological membranes and with the voltage-gated sodium channel, Quim. Nova 31 (2008) 1775-1783.

[23] K. Simons, E. Ikonen, Functional rafts in cell membranes, Nature 387 (1997) 569-572.

[24] D.A. Brown, E. London, Functions of lipid rafts in biological membranes, Annu. Rev. Cell Dev. Biol. 14 (1998) 111-136.

[25] B. Ramstedt, J.P. Slotte, Sphingolipids and the formation of sterol-enriched ordered membrane domains, Biochim. Biophys. Acta-Biomembr. 1758 (2006) 1945-1956.

[26] G. Vereb, J. Szollosi, J. Matko, P. Nagy, T. Farkas, L. Vigh, L. Matyus, T.A. Waldmann, S. Damjanovich, Dynamic, yet structured: The cell membrane three decades after the Singer-Nicolson model, Proc. Natl. Acad. Sci. U. S. A. 100 (2003) 8053-8058.

[27] F. Olson, C.A. Hunt, F.C. Szoka, W.J. Vail, D. Papahadjopoulos, Preparation of liposomes of defined size distribution by extrusion through polycarbonate membranes, Biochim. Biophys. Acta 557 (1979) 9-23.

[28] E.G. Finer, A.G. Flook, H. Hauser, Mechanism of sonication of aqueous egg-yolk lecithin dispersions and nature of resultant particles, Biochim. Biophys. Acta 260 (1972) 49-58.

[29] M.I. Angelova, D.S. Dimitrov, Liposome electroformation, Faraday Discuss. 81 (1986) 303-311.

[30] L.A. Bagatolli, T. Parasassi, E. Gratton, Giant phospholipid vesicles: Comparison among the whole lipid sample characteristics using different preparation methods - a two photon fluorescence microscopy study, Chem. Phys. Lipids 105 (2000) 135-147.

[31] M. Montal, P. Mueller, Formation of bimolecular membranes from lipid monolayers and a study of their electrical properties, Proc. Natl. Acad. Sci. U. S. A. 69 (1972) 3561-3566.

[32] A. Horner, Y.N. Antonenko, P. Pohl, Coupled diffusion of peripherally bound

peptides along the outer and inner membrane leaflets, Biophys. J. 96 (2009) 2689-2695.

[33] E. Sackmann, Supported membranes: Scientific and practical applications, Science 271 (1996) 43-48.

[34] L.K. Tamm, H.M. Mcconnell, Supported phospholipid-bilayers, Biophys. J. 47 (1985) 105-113.

[35] I. Mey, M. Stephan, E.K. Schmitt, M.M. Müller, M. Ben Amar, C. Steinem, A. Janshoff, Local membrane mechanics of pore-spanning bilayers, J. Am. Chem. Soc. 131 (2009) 7031-7039.

[36] M.R. Nussio, G. Oncins, I. Ridelis, E. Szili, J.G. Shapter, F. Sanz, N.H. Voelcker, Nanomechanical characterization of phospholipid bilayer islands on flat and porous substrates: A force spectroscopy study, J. Phys. Chem. B 113 (2009) 10339-10347.

[37] A.A. Brian, H.M. McConnell, Allogeneic stimulation of cyto-toxic T-cells by supported planar membranes, P. Natl. Acad. Sci.-Biol. 81 (1984) 6159-6163.

[38] R. Richter, A. Mukhopadhyay, A. Brisson, Pathways of lipid vesicle deposition on solid surfaces: A combined QCM-D and AFM study, Biophys. J. 85 (2003) 3035-3047.

[39] R.P. Richter, R. Berat, A.R. Brisson, Formation of solid-supported lipid bilayers: An integrated view, Langmuir 22 (2006) 3497-3505.

[40] I. Reviakine, A. Brisson, Formation of supported phospholipid bilayers from unilamellar vesicles investigated by atomic force microscopy, Langmuir 16 (2000) 1806-1815.

[41] U. Seifert, Configurations of fluid membranes and vesicles, Adv. Phys. 46 (1997) 13-137.

[42] F.Y. Jiang, Y. Bouret, J.T. Kindt, Molecular dynamics simulations of the lipid bilayer edge, Biophys. J. 87 (2004) 182-192.

[43] C.A. Keller, K. Glasmästar, V.P. Zhdanov, B. Kasemo, Formation of supported membranes from vesicles, Phys. Rev. Lett. 84 (2000) 5443-5446.

[44] M. Beneš, D. Billy, A. Benda, H. Speijer, M. Hof, W.T. Hermens, Surface-dependent transitions during self-assembly of phospholipid membranes on mica, silica, and glass, Langmuir 20 (2004) 10129-10137.

[45] E. Reimhult, F. Hook, B. Kasemo, Vesicle adsorption on SiO2 and TiO2: Dependence on vesicle size, J. Chem. Phys. 117 (2002) 7401-7404.

[46] P.S. Cremer, S.G. Boxer, Formation and spreading of lipid bilayers on planar glass supports, J. Phys. Chem. B 103 (1999) 2554-2559.

[47] P.B. Contino, C.A. Hasselbacher, J.B.A. Ross, Y. Nemerson, Use of an oriented transmembrane protein to probe the assembly of a supported phospholipid-bilayer, Biophys. J. 67 (1994) 1113-1116.

[48] E. Reimhult, B. Kasemo, F. Hook, Rupture pathway of phosphatidylcholine liposomes on silicon dioxide, International Journal of Molecular Sciences 10 (2009) 1683-1696.

[49] R. Richter, The formation of solid-supported lipid membranes and two-dimensional assembly of proteins. (disertation thesis), Université Bordeaux I,

Pessac, 2004.

[50] J. Rädler, H. Strey, E. Sackmann, Phenomenology and kinetics of lipid bilayer spreading on hydrophilic surfaces, Langmuir 11 (1995) 4539-4548.

[51] R.P. Richter, A. Brisson, Characterization of lipid bilayers and protein assemblies supported on rough surfaces by atomic force microscopy, Langmuir 19 (2003) 1632-1640.

[52] M. Hetzer, S. Heinz, S. Grage, T.M. Bayerl, Asymmetric molecular friction in supported phospholipid bilayers revealed by NMR measurements of lipid diffusion, Langmuir 14 (1998) 982-984.

[53] L.J. Lis, M. McAlister, N. Fuller, R.P. Rand, V.A. Parsegian, Interactions between neutral phospholipid-bilayer membranes, Biophys. J. 37 (1982) 657-665.

[54] M. Przybylo, J. Sýkora, J. Humpolíčková, A. Benda, A. Zan, M. Hof, Lipid diffusion in giant unilamellar vesicles is more than 2 times faster than in supported phospholipid bilayers under identical conditions, Langmuir 22 (2006) 9096-9099.

[55] L.T. Mimms, G. Zampighi, Y. Nozaki, C. Tanford, J.A. Reynolds, Phospholipid vesicle formation and transmembrane protein incorporation using octyl glucoside, Biochemistry 20 (1981) 833-840.

[56] R.M.A. Azzam, N.M. Bashara, Ellipsometry and polarized light, 2nd ed., Elsevier, Amsterdam, 1987.

[57] F.L. McCrackin, E. Passaglia, R.R. Stromberg, H.L. Steinberg, Measurement of thickness and refractive index of very thin films and optical properties of surfaces by ellipsometry, J. Res. Natl. Inst. Stand. Technol. A A 67 (1963) 363-377.

[58] P.A. Cuypers, J.W. Corsel, M.P. Janssen, J.M.M. Kop, W.T. Hermens, H.C. Hemker, The adsorption of prothrombin to phosphatidylserine multilayers quantitated by ellipsometry, J. Biol. Chem. 258 (1983) 2426-2431.

[59] M. Born, E. Wolf, Principles of optics, Pergamon Press, New York, 1965.

[60] J.A. Woollam, B. Johs, C. Herzinger, J. Hilfiker, R. Synowicki, C. Bungay, Overview of variable angle spectroscopic ellipsometry (VASE), part i: Basic theory and typical applications, SPIE Proceedings CR72 (1999) 3-28.

[61] J.A. Woollam, B. Johs, C. Herzinger, J. Hilfiker, R. Synowicki, C. Bungay, Overview of variable angle spectroscopic ellipsometry (VASE), part ii: Advanced applications, SPIE Proceedings CR72 (1999) 29-58.

[62] P.A. Cuypers, W.T. Hermens, H.C. Hemker, Ellipsometry as a tool to study protein films at liquid-solid interfaces, Anal. Biochem. 84 (1978) 56-67.

[63] P.L.A. Giesen, G.M. Willems, H.C. Hemker, M.C.A. Stuart, W.T. Hermens, Monitoring of unbound protein in vesicle suspensions with off-null ellipsometry, Biochim. Biophys. Acta 1147 (1993) 125-131.

[64] L. Ringstad, A. Schmidtchen, M. Malmsten, Effect of peptide length on the interaction between consensus peptides and DOPC/DOPA bilayers, Langmuir 22 (2006) 5042-5050.

[65] H.I. Petrache, S. Tristram-Nagle, K. Gawrisch, D. Harries, V.A. Parsegian,

J.F. Nagle, Structure and fluctuations of charged phosphatidylserine bilayers in the absence of salt, Biophys. J. 86 (2004) 1574-1586.

[66] H.I. Petrache, S. Tristram-Nagle, J.F. Nagle, Fluid phase structure of EPC and DMPC bilayers, Chem. Phys. Lipids 95 (1998) 83-94.

[67] M. Grandbois, H. Clausen-Schaumann, H. Gaub, Atomic force microscope imaging of phospholipid bilayer degradation by phospholipase A_2, Biophys. J. 74 (1998) 2398-2404.

[68] J.T. Marques, A.S. Viana, R.F.M. De Almeida, Ethanol effects on binary and ternary supported lipid bilayers with gel/fluid domains and lipid rafts, Biochim. Biophys. Acta-Biomembr. 1808 (2011) 405-414.

[69] J.X. Mou, J. Yang, C. Huang, Z.F. Shao, Alcohol induces interdigitated domains in unilamellar phosphatidylcholine bilayers, Biochemistry 33 (1994) 9981-9985.

[70] T.V. Ratto, M.L. Longo, Obstructed diffusion in phase-separated supported lipid bilayers: A combined atomic force microscopy and fluorescence recovery after photobleaching approach, Biophys. J. 83 (2002) 3380-3392.

[71] J. Jass, T. Tjarnhage, G. Puu, From liposomes to supported, planar bilayer structures on hydrophilic and hydrophobic surfaces: An atomic force microscopy study, Biophys. J. 79 (2000) 3153-3163.

[72] S.J. Johnson, T.M. Bayerl, D.C. Mcdermott, G.W. Adam, A.R. Rennie, R.K. Thomas, E. Sackmann, Structure of an adsorbed dimyristoylphosphatidylcholine bilayer measured with specular reflection of neutrons, Biophys. J. 59 (1991) 289-294.

[73] T.M. Bayerl, M. Bloom, Physical-properties of single phospholipid-bilayers adsorbed to micro glass-beads - a new vesicular model system studied by ^{2}H-nuclear magnetic-resonance, Biophys. J. 58 (1990) 357-362.

[74] A. Miszta, B. van Deursen, R. Schoufs, M. Hof, W.T. Hermens, Absence of ethanol-induced interdigitation in supported phospholipid bilayers on silica surfaces, Langmuir 24 (2008) 19-21.

[75] T. Steinberger, Upgrading an existing null ellipsometer. Application of this setup for characterization of membrane activity of antibacterial peptides. (diploma thesis), Czech Technical University in Prague, Kladno, 2009.

[76] M.C. Howland, A.N. Parikh, Model studies of membrane disruption by photogenerated oxidative assault, J. Phys. Chem. B 114 (2010) 6377-6385.

[77] G. Puu, I. Gustafson, Planar lipid bilayers on solid supports from liposomes - factors of importance for kinetics and stability, Biochim. Biophys. Acta-Biomembr. 1327 (1997) 149-161.

[78] E.M.A. Pereira, D.F.S. Petri, A.M. Carmona-Ribeiro, Adsorption of cationic lipid bilayer onto flat silicon wafers: Effect of ion nature and concentration, J. Phys. Chem. B 110 (2006) 10070-10074.

[79] D. Stroumpoulis, A. Parra, M. Tirrell, A kinetic study of vesicle fusion on silicon dioxide surfaces by ellipsometry, AIChE J. 52 (2006) 2931-2937.

[80] S. Faiss, S. Schuy, D. Weiskopf, C. Steinem, A. Janshoff, Phase transition of individually addressable microstructured membranes visualized by imaging ellipsometry, J. Phys. Chem. B 111 (2007) 13979-13986.

[81] N.M. Peachey, C.J. Eckhardt, Structural studies of ordered monolayers using atomic-force microscopy, Micron 25 (1994) 271-292.

[82] A.L. Weisenhorn, M. Egger, F. Ohnesorge, S.A.C. Gould, S.P. Heyn, H.G. Hansma, R.L. Sinsheimer, H.E. Gaub, P.K. Hansma, Molecular-resolution images of Langmuir-Blodgett-films and DNA by atomic force microscopy, Langmuir 7 (1991) 8-12.

[83] Y.F. Dufrene, G.U. Lee, Advances in the characterization of supported lipid films with the atomic force microscope, Biochim. Biophys. Acta-Biomembr. 1509 (2000) 14-41.

[84] V. Oliynyk, U. Kaatze, T. Heimburg, Defect formation of lytic peptides in lipid membranes and their influence on the thermodynamic properties of the pore environment, Biochim. Biophys. Acta-Biomembr. 1768 (2007) 236-245.

[85] N.C. Santos, M. Castanho, An overview of the biophysical applications of atomic force microscopy, Biophys. Chem. 107 (2004) 133-149.

[86] S.F. Ahmad, L.A. Chtcheglova, B. Mayer, S.A. Kuznetsov, P. Hinterdorfer, Nanosensing of Fc gamma receptors on macrophages, Anal. Bioanal. Chem. 399 (2011) 2359-2367.

[87] P.K. Hansma, J.P. Cleveland, M. Radmacher, D.A. Walters, P.E. Hillner, M. Bezanilla, M. Fritz, D. Vie, H.G. Hansma, C.B. Prater, J. Massie, L. Fukunaga, J. Gurley, V. Elings, Tapping mode atomic-force microscopy in liquids, Appl. Phys. Lett. 64 (1994) 1738-1740.

[88] M. Wadsak, M. Schreiner, T. Aastrup, C. Leygraf, A comparison of preparation methods of copper surfaces for in situ scanning force microscopy investigations, Appl. Surf. Sci. 157 (2000) 39-46.

[89] J. Yang, Z.F. Shao, Recent advances in biological atomic-force microscopy, Micron 26 (1995) 35-49.

[90] M. Meincken, D.L. Holroyd, M. Rautenbach, Atomic force microscopy study of the effect of antimicrobial peptides on the cell envelope of Escherichia coli, Antimicrob. Agents Chemother. 49 (2005) 4085-4092.

[91] B.P. Jena, Cell secretion machinery: Studies using the AFM, Ultramicroscopy 106 (2006) 663-669.

[92] J. Andrä, I. Jakovkin, J. Grotzinger, O. Hecht, A.D. Krasnosdembskaya, T. Goldmann, T. Gutsmann, M. Leippe, Structure and mode of action of the antimicrobial peptide arenicin, Biochem. J. 410 (2008) 113-122.

[93] T. Viitala, J. Peltonen, UV-induced reaction kinetics of dilinoleoylphosphatidylethanolamine monolayers, Biophys. J. 76 (1999) 2803-2813.

[94] A. Mecke, D.K. Lee, A. Ramamoorthy, B.G. Orr, M.M.B. Holl, Membrane thinning due to antimicrobial peptide binding: An atomic force microscopy study of MSI-78 in lipid bilayers, Biophys. J. 89 (2005) 4043-4050.

[95] Z.V. Leonenko, E. Finot, H. Ma, T.E.S. Dahms, D.T. Cramb, Investigation of temperature-induced phase transitions in POPC and DPPC phospholipid bilayers using temperature-controlled scanning force microscopy, Biophys. J. 86 (2004) 3783-3793.

[96] S. Chiantia, N. Kahya, J. Ries, P. Schwille, Effects of ceramide on liquid-

ordered domains investigated by simultaneous AFM and FCS, Biophys. J. 90 (2006) 4500-4508.

[97] L. Zhang, R. Vidu, A.J. Waring, R.I. Lehrer, M.L. Longo, P. Stroeve, Electrochemical and surface properties of solid-supported, mobile phospholipid bilayers on a polyion/alkylthiol layer pair used for detection of antimicrobial peptide insertion, Langmuir 18 (2002) 1318-1331.

[98] B. Windschiegl, A. Orth, W. Romer, L. Berland, B. Stechmann, P. Bassereau, L. Johannes, C. Steinem, Lipid reorganization induced by shiga toxin clustering on planar membranes, PLoS One 4 (2009) e6238.

[99] R.P. Richter, J.L.K. Him, B. Tessier, C. Tessier, A.R. Brisson, On the kinetics of adsorption and two-dimensional self-assembly of annexin A5 on supported lipid bilayers, Biophys. J. 89 (2005) 3372-3385.

[100] A. Diaspro (Ed.), Confocal and two-photon microscopy: Foundations, applications, and advances, Wiley, New York, 2002.

[101] J. Plášek, Konfokální mikroskop, Vesmír 74 (1995) 508-510.

[102] J. Enderlein, I. Gregor, D. Patra, T. Dertinger, U.B. Kaupp, Performance of fluorescence correlation spectroscopy for measuring diffusion and concentration, ChemPhysChem 6 (2005) 2324-2336.

[103] J. Enderlein, I. Gregor, D. Patra, J. Fitter, Art and artefacts of fluorescence correlation spectroscopy, Curr. Pharm. Biotechnol. 5 (2004) 155-161.

[104] N.L. Thompson, Fluorescence correlation spectroscopy, in: J.R. Lakowicz (Ed.), Topics in fluorescence spectroscopy, vol. 1, Plenum Press, New York, 1991, pp. 337-378.

[105] J. Humpolíčková, A. Benda, R. Macháň, J. Enderlein, M. Hof, Dynamic saturation optical microscopy: Employing dark-state formation kinetics for resolution enhancement, Phys. Chem. Chem. Phys. 12 (2010) 12457-12465.

[106] T. Dertinger, V. Pacheco, I. von der Hocht, R. Hartmann, I. Gregor, J. Enderlein, Two-focus fluorescence correlation spectroscopy: A new tool for accurate and absolute diffusion measurements, ChemPhysChem 8 (2007) 433-443.

[107] J.P. Skinner, Y. Chen, J.D. Muller, Fluorescence fluctuation spectroscopy in the presence of immobile fluorophores, Biophys. J. 94 (2008) 2349-2360.

[108] R. Rigler, U. Mets, J. Widengren, P. Kask, Fluorescence correlation spectroscopy with high count rate and low background: Analysis of translational diffusion, Eur. Biophys. J. 22 (1993) 169-175.

[109] S.M. Sorscher, M.P. Klein, Profile of a focused collimated laser-beam near the focal minimum characterized by fluorescence correlation spectroscopy, Rev. Sci. Instrum. 51 (1980) 98-102.

[110] J. Enderlein, I. Gregor, D. Patra, J. Fitter, Statistical analysis of diffusion coefficient determination by fluorescence correlation spectroscopy, J. Fluoresc. 15 (2005) 415-422.

[111] H. Qian, E.L. Elson, Analysis of confocal laser-microscope optics for 3-D fluorescence correlation spectroscopy, Appl. Optics 30 (1991) 1185-1195.

[112] S.T. Hess, W.W. Webb, Focal volume optics and experimental artifacts in

confocal fluorescence correlation spectroscopy, Biophys. J. 83 (2002) 2300-2317.

[113] J. Enderlein, Theoretical study of detection of a dipole emitter through an objective with high numerical aperture, Opt. Lett. 25 (2000) 634-636.

[114] J. Enderlein, W.P. Ambrose, Optical collection efficiency function in single-molecule detection experiments, Appl. Optics 36 (1997) 5298-5302.

[115] N.S. Claxton, T.J. Fellers, M.W. Davidson, Laser scanning confocal microscopy, Olympus Corporation, Tokyo, 2005.

[116] S. Wilhelm, B. Gröbler, M. Gluch, H. Heinz, Confocal laser scanning microscopy: Optical image formation and electronic signal processing, Carl Zeiss, Jena, 2003.

[117] K. Carlsson, The influence of specimen refractive-index, detector signal integration, and nonuniform scan speed on the imaging properties in confocal microscopy, J. Microsc.-Oxf. 163 (1991) 167-178.

[118] T. Damm, B. Wilhelmi, Optimum recording conditions in scanning microscopes, J. Microsc.-Oxf. 165 (1992) 71-80.

[119] T.A. Klar, M. Dyba, S.W. Hell, Stimulated emission depletion microscopy with an offset depleting beam, Appl. Phys. Lett. 78 (2001) 393-395.

[120] B. Harke, J. Keller, C.K. Ullal, V. Westphal, A. Schoenle, S.W. Hell, Resolution scaling in STED microscopy, Opt. Express 16 (2008) 4154-4162.

[121] E. Rittweger, K.Y. Han, S.E. Irvine, C. Eggeling, S.W. Hell, STED microscopy reveals crystal colour centres with nanometric resolution, Nat. Photonics 3 (2009) 144-147.

[122] D. Wildanger, J. Buckers, V. Westphal, S.W. Hell, L. Kastrup, A STED microscope aligned by design, Opt. Express 17 (2009) 16100-16110.

[123] M. Leutenegger, C. Eggeling, S.W. Hell, Analytical description of STED microscopy performance, Opt. Express 18 (2010) 26417-26429.

[124] J. Humpolíčková, A. Benda, J. Enderlein, Optical saturation as a versatile tool to enhance resolution in confocal microscopy, Biophys. J. 97 (2009) 2623-2629.

[125] J. Enderlein, Breaking the diffraction limit with dynamic saturation optical microscopy, Appl. Phys. Lett. 87 (2005) 094105.

[126] R.P. Haugland, The handbook - a guide to fluorescent probes and labelling technologies, 10th ed., Invitrogen Corporation, Carlsbad, 2005.

[127] A. Benda, M. Beneš, V. Mareček, A. Lhotský, W.T. Hermens, M. Hof, How to determine diffusion coefficients in planar phospholipid systems by confocal fluorescence correlation spectroscopy, Langmuir 19 (2003) 4120-4126.

[128] A. Benda, V. Fagul'ova, A. Deyneka, J. Enderlein, M. Hof, Fluorescence lifetime correlation spectroscopy combined with lifetime tuning: New perspectives in supported phospholipid bilayer research, Langmuir 22 (2006) 9580-9585.

[129] E. Elson, D. Magde, Fluorescence correlation spectroscopy. I. Conceptual basis and theory, Biopolymers 13 (1974) 1-27.

[130] D. Magde, E. Elson, W.W. Webb, Thermodynamic fluctuations in a reacting system - measurement by fluorescence correlation spectroscopy, Phys. Rev. Lett. 29 (1972) 705-708.

[131] D. Magde, E. Elson, Fluorescence correlation spectroscopy. II. An experimental realization, Biopolymers 13 (1974) 29-61.

[132] T. Wohland, R. Rigler, H. Vogel, The standard deviation in fluorescence correlation spectroscopy, Biophys. J. 80 (2001) 2987-2999.

[133] J. Sýkora, K. Kaiser, I. Gregor, W. Bönigk, G. Schmalzing, J. Enderlein, Exploring fluorescence antibunching in solution to determine the stoichiometry of molecular complexes, Anal. Chem. 79 (2007) 4040-4049.

[134] J.R. Lakowicz, Principles of fluorescence spectrosopy, 3rd ed., Springer, New York, 2006.

[135] J. Widengren, U. Mets, R. Rigler, Fluorescence correlation spectroscopy of triplet-states in solution - a theoretical and experimental-study, J. Phys. Chem. 99 (1995) 13368-13379.

[136] J. Widengren, R. Rigler, Review - fluorescence correlation spectroscopy as a tool to investigate chemical reactions in solutions and on cell surfaces, Cell. Mol. Biol. 44 (1998) 857-879.

[137] P. Schwille, J. Bieschke, F. Oehlenschlager, Kinetic investigations by fluorescence correlation spectroscopy: The analytical and diagnostic potential of diffusion studies, Biophys. Chem. 66 (1997) 211-228.

[138] P. Schwille, F.J. Meyer-Almes, R. Rigler, Dual-color fluorescence cross-correlation spectroscopy for multicomponent diffusional analysis in solution, Biophys. J. 72 (1997) 1878-1886.

[139] E.L. Elson, Fluorescence correlation spectroscopy and photobleaching recovery, Annu. Rev. Phys. Chem. 36 (1985) 379-406.

[140] R. Šachl, I. Mikhalyov, M. Hof, L.B.A. Johansson, A comparative study on ganglioside micelles using electronic energy transfer, fluorescence correlation spectroscopy and light scattering techniques, Phys. Chem. Chem. Phys. 11 (2009) 4335-4343.

[141] L. Yu, J.L. Ding, B. Ho, T. Wohland, Investigation of a novel artificial antimicrobial peptide by fluorescence correlation spectroscopy: An amphipathic cationic pattern is sufficient for selective binding to bacterial type membranes and antimicrobial activity, Biochim. Biophys. Acta-Biomembr. 1716 (2005) 29-39.

[142] P. Kask, R. Günther, P. Axhausen, Statistical accuracy in fluorescence fluctuation experiments, Eur. Biophys. J. Biophys. Lett. 25 (1997) 163-169.

[143] P. Schwille, K.G. Heinze, Two-photon fluorescence cross-correlation spectroscopy, ChemPhysChem 2 (2001) 269-272.

[144] L. Guo, J.Y. Har, J. Sankaran, Y.M. Hong, B. Kannan, T. Wohland, Molecular diffusion measurement in lipid bilayers over wide concentration ranges: A comparative study, ChemPhysChem 9 (2008) 721-728.

[145] J. Ries, P. Schwille, New concepts for fluorescence correlation spectroscopy on membranes, Phys. Chem. Chem. Phys. 10 (2008) 3487-3497.

[146] D.E. Koppel, Statistical accuracy in fluorescence correlation spectroscopy, Phys. Rev. A 10 (1974) 1938-1945.

[147] H. Qian, On the statistics of fluorescence correlation spectroscopy, Biophys. Chem. 38 (1990) 49-57.

[148] I. Gregor, D. Patra, J. Enderlein, Optical saturation in fluorescence correlation spectroscopy under continuous-wave and pulsed excitation, ChemPhysChem 6 (2005) 164-170.

[149] Z. Petrášek, P. Schwille, Photobleaching in two-photon scanning fluorescence correlation spectroscopy, ChemPhysChem 9 (2008) 147-158.

[150] J. Widengren, R. Rigler, Mechanism of photobleaching investigated by fluorescence correlation spectroscopy, Bioimaging 4 (1996) 149-157.

[151] J. Enderlein, I. Gregor, Using fluorescence lifetime for discriminating detector afterpulsing in fluorescence-correlation spectroscopy, Rev. Sci. Instrum. 76 (2005) 033102.

[152] P. Kapusta, M. Wahl, A. Benda, M. Hof, J. Enderlein, Fluorescence lifetime correlation spectroscopy, J. Fluoresc. 17 (2007) 43-48.

[153] J. Humpolíčková, A. Benda, J. Sýkora, R. Macháň, T. Kral, B. Gasinska, J. Enderlein, M. Hof, Equilibrium dynamics of spermine-induced plasmid DNA condensation revealed by fluorescence lifetime correlation spectroscopy, Biophys. J. 94 (2008) L17-L19.

[154] M. Wahl, I. Gregor, M. Patting, J. Enderlein, Fast calculation of fluorescence correlation data with asynchronous time-correlated single-photon counting, Opt. Express 11 (2003) 3583-3591.

[155] A. Benda, M. Hof, M. Wahl, M. Patting, R. Erdmann, P. Kapusta, TCSPC upgrade of a confocal FCS microscope, Rev. Sci. Instrum. 76 (2005) 033106.

[156] A. Benda, New posibilities in fluorescence correlation spectroscopy. (disertation thesis), Charles University, Prague, 2006.

[157] M. Beneš, D. Billy, W.T. Hermens, M. Hof, Muscovite (mica) allows the characterisation of supported bilayers by ellipsometry and confocal fluorescence correlation spectroscopy, Biol. Chem. 383 (2002) 337-341.

[158] S. Milon, R. Hovius, H. Vogel, T. Wohland, Factors influencing fluorescence correlation spectroscopy measurements on membranes: Simulations and experiments, Chem. Phys. 288 (2003) 171-186.

[159] N. Malchus, M. Weiss, Elucidating anomalous protein diffusion in living cells with fluorescence correlation spectroscopy-facts and pitfalls, J. Fluoresc. 20 (2010) 19-26.

[160] T.V. Ratto, M.L. Longo, Anomalous subdiffusion in heterogeneous lipid bilayers, Langmuir 19 (2003) 1788-1793.

[161] W.L.C. Vaz, R.M. Clegg, D. Hallmann, Translational diffusion of lipids in liquid-crystalline phase phosphatidylcholine multibilayers - a comparison of experiment with theory, Biochemistry 24 (1985) 781-786.

[162] P.F.F. Almeida, W.L.C. Vaz, T.E. Thompson, Lateral diffusion in the liquid-phases of dimyristoylphosphatidylcholine cholesterol lipid bilayers - a free-volume analysis, Biochemistry 31 (1992) 6739-6747.

[163] M.A. Deverall, E. Gindl, E.K. Sinner, H. Besir, J. Ruehe, M.J. Saxton, C.A. Naumann, Membrane lateral mobility obstructed by polymer-tethered lipids studied at the single molecule level, Biophys. J. 88 (2005) 1875-1886.

[164] M.J. Saxton, Anomalous diffusion due to obstacles - a monte-carlo study, Biophys. J. 66 (1994) 394-401.

[165] L. Wawrezinieck, H. Rigneault, D. Marguet, P.F. Lenne, Fluorescence correlation spectroscopy diffusion laws to probe the submicron cell membrane organization, Biophys. J. 89 (2005) 4029-4042.

[166] J. Wenger, H. Rigneault, J. Dintinger, D. Marguet, P.F. Lenne, Single-fluorophore diffusion in a lipid membrane over a subwavelength aperture, J. Biol. Phys. 32 (2006) SN1-SN4.

[167] J. Wenger, F. Conchonaud, J. Dintinger, L. Wawrezinieck, T.W. Ebbesen, H. Rigneault, D. Marguet, P.F. Lenne, Diffusion analysis within single nanometric apertures reveals the ultrafine cell membrane organization, Biophys. J. 92 (2007) 913-919.

[168] J. Humpolíčková, E. Gielen, A. Benda, V. Faguľova, J. Vercammen, M. Vandeven, M. Hof, M. Ameloot, Y. Engelborghs, Probing diffusion laws within cellular membranes by Z-scan fluorescence correlation spectroscopy, Biophys. J. 91 (2006) L23-L25.

[169] C. Eggeling, C. Ringemann, R. Medda, G. Schwarzmann, K. Sandhoff, S. Polyakova, V.N. Belov, B. Hein, C. von Middendorff, A. Schonle, S.W. Hell, Direct observation of the nanoscale dynamics of membrane lipids in a living cell, Nature 457 (2009) 1159-1163.

[170] R.E.W. Hancock, M.G. Scott, The role of antimicrobial peptides in animal defenses, Proc. Natl. Acad. Sci. U. S. A. 97 (2000) 8856-8861.

[171] B. Yasin, M. Pang, J.S. Turner, Y. Cho, N.N. Dinh, A.J. Waring, R.I. Lehrer, E.A. Wagar, Evaluation of the inactivation of infectious herpes simplex virus by host-defense peptides, Eur. J. Clin. Microbiol. Infect. Dis. 19 (2000) 187-194.

[172] K. Matsuzaki, Why and how are peptide-lipid interactions utilized for self-defense? Magainins and tachyplesins as archetypes, Biochim. Biophys. Acta-Biomembr. 1462 (1999) 1-10.

[173] D.A. Steinberg, M.A. Hurst, C.A. Fujii, A.H.C. Kung, J.F. Ho, F.C. Cheng, D.J. Loury, J.C. Fiddes, Protegrin-1: A broad-spectrum, rapidly microbicidal peptide with in vivo activity, Antimicrob. Agents Chemother. 41 (1997) 1738-1742.

[174] M. Salzet, Neuropeptide-derived antimicrobial peptides from invertebrates for biomedical applications, Curr. Med. Chem. 12 (2005) 3055-3061.

[175] R.A. Cruciani, J.L. Barker, M. Zasloff, H.C. Chen, O. Colamonici, Antibiotic magainins exert cytolytic activity against transformed-cell lines through channel formation, Proc. Natl. Acad. Sci. U. S. A. 88 (1991) 3792-3796.

[176] J. Lehmann, M. Retz, S.S. Sidhu, H. Suttmann, M. Sell, F. Paulsen, J. Harder, G. Unteregger, M. Stockle, Antitumor activity of the antimicrobial peptide magainin II against bladder cancer cell lines, Eur. Urol. 50 (2006) 141-147.

[177] P. Limjaroen, E. Ryser, H. Lockhart, B. Harte, Development of a food

packaging coating material with antimicrobial properties, J. Plast. Film Sheeting 19 (2003) 95-109.

[178] T. Rydlo, J. Miltz, A. Mor, Eukaryotic antimicrobial peptides: Promises and premises in food safety, J. Food Sci. 71 (2006) R125-R135.

[179] Y.P. Zhang, R. Lewis, G.D. Henry, B.D. Sykes, R.S. Hodges, R.N. McElhaney, Peptide models of helical hydrophobic transmembrane segments of membrane-proteins .1. Studies of the conformation, intrabilayer orientation, and amide hydrogen exchangeability of Ac-K_2-$(LA)_{12}$-K_2-amide, Biochemistry 34 (1995) 2348-2361.

[180] T. Sheynis, J. Sýkora, A. Benda, S. Kolusheva, M. Hof, R. Jelinek, Bilayer localization of membrane-active peptides studied in biomimetic vesicles by visible and fluorescence spectroscopies, European Journal of Biochemistry 270 (2003) 4478-4487.

[181] B. Bechinger, Towards membrane protein design: pH-sensitive topology of histidine-containing polypeptides, J. Mol. Biol. 263 (1996) 768-775.

[182] D. Wade, A. Boman, B. Wahlin, C.M. Drain, D. Andreu, H.G. Boman, R.B. Merrifield, All-d amino acid-containing channel-forming antibiotic peptides, Proc. Natl. Acad. Sci. U. S. A. 87 (1990) 4761-4765.

[183] K. Matsuzaki, K. Sugishita, M. Harada, N. Fujii, K. Miyajima, Interactions of an antimicrobial peptide, magainin 2, with outer and inner membranes of gram-negative bacteria, Biochim. Biophys. Acta-Biomembr. 1327 (1997) 119-130.

[184] R.M. Epand, H.J. Vogel, Diversity of antimicrobial peptides and their mechanisms of action, Biochim. Biophys. Acta-Biomembr. 1462 (1999) 11-28.

[185] M. Dathe, T. Wieprecht, Structural features of helical antimicrobial peptides: Their potential to modulate activity on model membranes and biological cells, Biochim. Biophys. Acta-Biomembr. 1462 (1999) 71-87.

[186] B. Bechinger, K. Lohner, Detergent-like actions of linear amphipathic cationic antimicrobial peptides, Biochim. Biophys. Acta-Biomembr. 1758 (2006) 1529-1539.

[187] B. Bechinger, The structure, dynamics and orientation of antimicrobial peptides in membranes by multidimensional solid-state NMR spectroscopy, Biochim. Biophys. Acta-Biomembr. 1462 (1999) 157-183.

[188] K. Matsuzaki, S. Yoneyama, K. Miyajima, Pore formation and translocation of melittin, Biophys. J. 73 (1997) 831-838.

[189] K. Matsuzaki, O. Murase, N. Fujii, K. Miyajima, Translocation of a channel-forming antimicrobial peptide, magainin-2, across lipid bilayers by forming a pore, Biochemistry 34 (1995) 6521-6526.

[190] L. Yang, T.A. Harroun, T.M. Weiss, L. Ding, H.W. Huang, Barrel-stave model or toroidal model? A case study on melittin pores, Biophys. J. 81 (2001) 1475-1485.

[191] H. Sato, J.B. Feix, Peptide-membrane interactions and mechanisms of membrane destruction by amphipathic alpha-helical antimicrobial peptides, Biochim. Biophys. Acta-Biomembr. 1758 (2006) 1245-1256.

[192] A.S. Ladokhin, S.H. White, 'detergent-like' permeabilization of anionic lipid vesicles by melittin, Biochim. Biophys. Acta-Biomembr. 1514 (2001) 253-260.

[193] S.E. Blondelle, K. Lohner, M.I. Aguilar, Lipid-induced conformation and lipid-binding properties of cytolytic and antimicrobial peptides: Determination and biological specificity, Biochim. Biophys. Acta-Biomembr. 1462 (1999) 89-108.

[194] H. Raghuraman, A. Chattopadhyay, Melittin: A membrane-active peptide with diverse functions, Biosci. Rep. 27 (2007) 189-223.

[195] A. Peschel, M. Otto, R.W. Jack, H. Kalbacher, G. Jung, F. Gotz, Inactivation of the dlt operon in staphylococcus aureus confers sensitivity to defensins, protegrins, and other antimicrobial peptides, J. Biol. Chem. 274 (1999) 8405-8410.

[196] P. Wessman, M. Morin, K. Reijmar, K. Edwards, Effect of alpha-helical peptides on liposome structure: A comparative study of melittin and alamethicin, J. Colloid Interface Sci. 346 (2010) 127-135.

[197] L.J. Zhang, R. Benz, R.E.W. Hancock, Influence of proline residues on the antibacterial and synergistic activities of alpha-helical peptides, Biochemistry 38 (1999) 8102-8111.

[198] Y.Q. Xiong, M.R. Yeaman, A.S. Bayer, In vitro antibacterial activities of platelet microbicidal protein and neutrophil defensin against staphylococcus aureus are influenced by antibiotics differing in mechanism of action, Antimicrob. Agents Chemother. 43 (1999) 1111-1117.

[199] D.P. Satchell, T. Sheynis, Y. Shirafuji, S. Kolusheva, A.J. Ouellette, R. Jelinek, Interactions of mouse paneth cell alpha-defensins and alpha-defensin precursors with membranes, J. Biol. Chem. 278 (2003) 13838-13846.

[200] A.J. Ouellette, M.E. Selsted, Paneth cell defensins: Endogenous peptide components of intestinal host defense, Faseb J. 10 (1996) 1280-1289.

[201] A.J. Ouellette, Paneth cell alpha-defensin synthesis and function, in: W.M. Shafer (Ed.), Antimicrobial peptides and human disease, vol. 306, Springer-Verlag Berlin, Berlin, 2006, pp. 1-25.

[202] D.P. Satchell, T. Sheynis, S. Kolusheva, J. Cummings, T.K. Vanderlick, R. Jelinek, M.E. Selsted, A.J. Ouellette, Quantitative interactions between cryptdin-4 amino terminal variants and membranes, Peptides 24 (2003) 1795-1805.

[203] M. Zasloff, B. Martin, H.C. Chen, Antimicrobial activity of synthetic magainin peptides and several analogs, Proc. Natl. Acad. Sci. U. S. A. 85 (1988) 910-913.

[204] R. Bucki, J.J. Pastore, P. Randhawa, R. Vegners, D.J. Weiner, P.A. Janmey, Antibacterial activities of rhodamine B-conjugated gelsolin-derived peptides compared to those of the antimicrobial peptides cathelicidin LL37, magainin II, and melittin, Antimicrob. Agents Chemother. 48 (2004) 1526-1533.

[205] T.C. Terwilliger, L. Weissman, D. Eisenberg, The structure of melittin in the form I crystals and its implication for melittin’s lytic and surface-activities, Biophys. J. 37 (1982) 353-361.

[206] K. Hristova, C.E. Dempsey, S.H. White, Structure, location, and lipid perturbations of melittin at the membrane interface, Biophys. J. 80 (2001) 801-811.

[207] M. Iwadate, T. Asakura, P.V. Dubovskii, H. Yamada, K. Akasaka, M.P. Williamson, Pressure-dependent changes in the structure of the melittin alpha-helix determined by NMR, J. Biomol. NMR 19 (2001) 115-124.

[208] T.V. Ovchinnikova, G.M. Aleshina, S.V. Balandin, A.D. Krasnosdembskaya, M.L. Markelov, E.I. Frolova, Y.F. Leonova, A.A. Tagaev, E.G. Krasnodembsky, V.N. Kokryakov, Purification and primary structure of two isoforms of arenicin, a novel antimicrobial peptide from marine polychaeta Arenicola marina, FEBS Lett. 577 (2004) 209-214.

[209] J. Andrä, M.U. Hammer, J. Grotzinger, I. Jakovkin, B. Lindner, E. Vollmer, H. Fedders, M. Leippe, T. Gutsmann, Significance of the cyclic structure and of arginine residues for the antibacterial activity of arenicin-1 and its interaction with phospholipid and lipopolysaccharide model membranes, Biol. Chem. 390 (2009) 337-349.

[210] A.J. Mason, C. Gasnier, A. Kichler, G. Prevost, D. Aunis, M.H. Metz-Boutigue, B. Bechinger, Enhanced membrane disruption and antibiotic action against pathogenic bacteria by designed histidine-rich peptides at acidic pH, Antimicrob. Agents Chemother. 50 (2006) 3305-3311.

[211] B. Bechinger, J.M. Ruysschaert, E. Goormaghtigh, Membrane helix orientation from linear dichroism of infrared attenuated total reflection spectra, Biophys. J. 76 (1999) 552-563.

[212] C. Aisenbrey, R. Kinder, E. Goormaghtigh, J.M. Ruysschaert, B. Bechinger, Interactions involved in the realignment of membrane-associated helices - an investigation using oriented solid-state NMR and attenuated total reflection fourier transform infrared spectroscopies, J. Biol. Chem. 281 (2006) 7708-7716.

[213] T.C.B. Vogt, B. Bechinger, The interactions of histidine-containing amphipathic helical peptide antibiotics with lipid bilayers - the effects of charges and pH, J. Biol. Chem. 274 (1999) 29115-29121.

[214] A. Pramanik, P. Thyberg, R. Rigler, Molecular interactions of peptide with phospholipid vesicle membranes as studied by fluorescence correlation spectroscopy, Chem. Phys. Lipids 104 (2000) 35-47.

[215] L.L. Yu, L. Guo, J.L. Ding, B. Ho, S.S. Feng, J. Popplewell, M. Swann, T. Wohland, Interaction of an artificial antimicrobial peptide with lipid membranes, Biochim. Biophys. Acta-Biomembr. 1788 (2009) 333-344.

[216] Y.A. Domanov, P.K.J. Kinnunen, Antimicrobial peptides temporins B and L induce formation of tubular lipid protrusions from supported phospholipid bilayers, Biophys. J. 91 (2006) 4427-4439.

[217] L.Y. Chen, J.J. Lin, C.W. Cheng, W.Y. Chen, Exploring the effect of cholesterol in lipid bilayer membrane on the melittin penetration mechanism, Anal. Biochem. 367 (2007) 49-55.

[218] S. Rex, Pore formation induced by the peptide melittin in different lipid vesicle membranes, Biophys. Chem. 58 (1996) 75-85.

[219] C. Steinem, H.J. Galla, A. Janshoff, Interaction of melittin with solid

supported membranes, Phys. Chem. Chem. Phys. 2 (2000) 4580-4585.

[220] T.V. Ovchinnikova, Z.O. Shenkarev, S.V. Balandin, K.D. Nadezhdin, A.S. Paramonov, V.N. Kokryakov, A.S. Arseniev, Molecular insight into mechanism of antimicrobial action of the beta-hairpin peptide arenicin: Specific oligomerization in detergent micelles, Biopolymers 89 (2008) 455-464.

[221] D. Sengupta, H. Leontiadou, A.E. Mark, S.J. Marrink, Toroidal pores formed by antimicrobial peptides show significant disorder, Biochim. Biophys. Acta-Biomembr. 1778 (2008) 2308-2317.

[222] M. Mally, J. Majhenc, S. Svetina, B. Zeks, The response of giant phospholipid vesicles to pore-forming peptide melittin, Biochim. Biophys. Acta-Biomembr. 1768 (2007) 1179-1189.

List of abbreviations

AFM	Atomic force microscopy
AMP	Antimicrobial peptide
DOPC	Dioleoyl-phosphatidylcholine
DOPG	Dioleoyl-phosphatidylglycerol
DOPS	Dioleoyl-phosphatidylserine
DSOM	Dynamic saturation optical microscopy
EDTA	Ethylenediaminetetraacetic acid
FCS	Fluorescence correlation spectroscopy
FLCS	Fluorescence lifetime correlation spectroscopy
FRAP	Fluorescence recovery after photobleaching
GUV	Giant unilamellar vesicle
HEPES	4-(2-hydroxyethyl)-1-piperazineethanesulfonic acid
LSM	Laser scanning microscopy
LUV	Large unilamellar vesicle
POPC	1-palmitoyl-2-oleoyl-phosphatdylcholine
POPG	1-palmitoyl-2-oleoyl-phosphatidylglycerol
SLB	Supported lipid bilayer
STED	Stimulated emission depletion
SUV	Small unilamellar vesicle
TCSPC	Time correlated single photon counting
TEM	Transverse electromagnetic mode
VASE	Variable angle spectroscopic ellipsometry

Attachments

Attachment I

Publication:

R. Macháň, M. Hof, *Lipid diffusion in planar membranes investigated by fluorescence correlation spectroscopy*, Biochim. Biophys. Acta-Biomembr. 1798 (2010) 1377-1391.

Attachment II

Publication:

A. Miszta, R. Macháň, A. Benda, A.J. Ouellette, W.T. Hermens, M. Hof, *Combination of ellipsometry, laser scanning microscopy and Z-scan fluorescence correlation spectroscopy elucidating interaction of cryptdin-4 with supported phospholipid bilayers*, J. Pept. Sci. 14 (2008) 503-509.

Attachment III

Publication:

R. Macháň, A. Miszta, W. Hermens, M. Hof, *Real-time monitoring of melittin-induced pore and tubule formation from supported lipid bilayers and its physiological relevance*, Chem. Phys. Lipids 163 (2010) 200-206.

Attachment IV

Publication:

R. Macháň, M. Hof, T. Chernovets, M.N. Zhmak, T.V. Ovchinnikova, J. Sýkora, *Formation of arenicin-1 microdomains in bilayers and their specific lipid interaction revealed by Z-scan FCS,* Anal. Bioanal. Chem. 399 (2011) 3547-3554.

Attachment V

Manuscript in Preparation:

Radek Macháň, Piotr Jurkiewicz, Tomáš Steinberger, Arnaud Marquette, Burkhard Bechinger, Martin Hof, *pH dependent binding of LAH_4 to large unilamellar vesicles: A fluorescence study*.